# The Prediction of Near-Field Jet Cross-Spectra

Steven A. E. Miller*

*The National Aeronautics and Space Administration*

**A prediction method is developed based on the acoustic analogy for the cross-power spectral density in the convecting near-field of compressible fluid turbulence. Equivalent source near-field, mid-field and far-field terms within the model integrand create corresponding near-field, mid-field, and far-field radiating waves. These equivalent sources are modeled with a single equation for the two-point cross-correlation of the Lighthill stress tensor that is dependent on the jet operating conditions. An alternative equivalent source model based on steady Reynolds-averaged Navier-Stokes solutions is proposed in the appendix. The cross-power spectral density model automatically reduces to a traditional auto-power spectral density model when observers are at the same location. Predictions of radiation intensity and coherence compare favorably with measurement in the near-field, mid-field, and far-field for a wide range of jet Mach numbers and temperature ratios.**

## Nomenclature

Symbols

| | |
|---|---|
| $A_i$ | Terms of the two-point cross-correlation |
| $A_{ijlm}$ | Coefficient matrix |
| $a_v$ | Number of averages |
| $a_{ij}, a_{lm}$ | Coefficients of $A_{ijlm}$ |
| $b_w$ | Bandwidth |
| $c$ | Speed of sound |
| $D$ | Jet diameter |
| $D_j$ | Fully expanded jet diameter |
| $e_s$ | Number of ensembles |
| $F_t$ | Far-field integrand terms |
| $f$ | Frequency |
| $G$ | Cross-power spectral density |
| $g$ | Green's function |
| $k$ | Turbulent kinetic energy |
| $l_{si}$ | Turbulent length scale |
| $M$ | Mach number |
| $M_c$ | Convective Mach number coefficient |
| $M_d$ | Design Mach number |
| $M_j$ | Fully expanded Mach number |
| $M_t$ | Mid-field integrand terms |
| $M_{\infty,i}$ | Component of the vector free-stream Mach number |
| $N_t$ | Near-field integrand terms |
| $P_f$ | Prefactor |
| $Pr$ | Prandtl number |
| $Pr_t$ | Turbulent Prandtl number |
| $p$ | Pressure |
| $R$ | Magnitude of $\boldsymbol{x}$ |
| $R_g$ | Gas constant |
| $R_{ijlm}$ | Two-point cross-correlation of $T_{ij}$ |
| $\boldsymbol{r}$ | Source vector |
| $S$ | Spectral density |
| $S_y$ | Equivalent spatial source distribution |
| $S_{ij}$ | Source tensor |
| $St$ | Strouhal number |
| $T_j$ | Fully expanded temperature |
| $T_{ij}$ | Lighthill stress tensor |
| $t$ | Time |
| $u$ | Velocity vector |
| $u_j$ | Fully expanded jet velocity |
| $\boldsymbol{x}$ | Observer spatial coordinate |
| $\boldsymbol{y}$ | Source spatial coordinate |
| $y_c$ | Core length |
| $\alpha$ | Constant length scale coefficient |
| $\beta_s$ | Constant amplification coefficient |
| $\delta$ | Dirac delta function |
| $\delta_{ij}$ | Kronecker delta function |
| $\boldsymbol{\eta}(\xi, \eta, \zeta)$ | Vector within source region |
| $\epsilon$ | Dissipation of turbulent kinetic energy |
| $\Gamma$ | Coherence |
| $\gamma$ | Ratio of specific heats |
| $\phi$ | Azimuthal observer angle |
| $\rho$ | Density |
| $\sigma$ | Anisotropic dependence parameter |
| $\sigma_f$ | Anisotropic amplification exponent |
| $\Psi$ | Inlet observer angle |
| $\tau$ | Retarded time |
| $\tau_s$ | Turbulent time scale |
| $\omega$ | Radial frequency |

Common Abbreviations

| | |
|---|---|
| CPSD | Cross-power spectral density, $G$ |
| PSD | Power spectral density |
| SHJAR | Small hot jet acoustic rig |
| SMC | Small metal chevron |
| SPL | Sound pressure level |
| TTR | Total temperature ratio |

*Research Aerospace Engineer, Aeroacoustics Branch, 2 N. Dryden St. Mail Stop 461, Hampton, VA 23681, AIAA Senior Member, s.miller@nasa.gov

## Introduction

Jet powered flight vehicles generate high intensity acoustic radiation that can have a negative impact on the surrounding community, military personnel, or can cause sonic fatigue. Accurate prediction of power spectral density (PSD) in the far-field has challenged mathematicians and scientists for well over 70 years. Prediction of cross-power spectral density (CPSD) in the jet near-field of a vehicle in flight is incredibly difficult. In this paper, a nearly analytical approach is proposed to predict the CPSD in the near-field from the turbulent mixing of a high-speed heated compressible jet. The developed model is general and can be applied to other flows if an appropriate expression of the two-point cross-correlation of Lighthill's stress tensor is known.

There are many current and future flight vehicle configurations that exhibit jet exhaust in close proximity to the airframe. This proximity induces interior noise and unsteady loading due to turbulence within the jet plume. Modern commercial aircraft cabin noise has many sources. One such source is the jet exhaust. General methods for cabin noise prediction are discussed by Vaicaitis[1] for a variety of external noise sources. The recently developed National Aeronautics and Space Administration (NASA) hybrid wing body aircraft (see Thomas et al.[2] and Czech et al.[3]) has engines located above the airframe. The nozzle exit is upstream of the airframe trailing edge and in some cases the jet exhaust directly impinges on the airframe trailing edge during take-off. Future NASA supersonic aircraft exhibit jet plumes either integrated or very close to the flight vehicle airframe (see Welge et al.[4,5] and Morgenstern et al.[6]). These vehicles will likely exhibit unique acoustic radiation and structural vibrations due to their engine placement.

Jet plumes produced by flight vehicles such as the McDonnell Douglas (now Boeing) F-15 Eagle and the Rockwell (also now Boeing) B-1B Lancer aircraft often exhibit extremely high loads near the engine exhaust that lead to sonic fatigue and possible flight vehicle failure. Seiner et al.,[7] for example, addressed this problem through modification of the geometry of the flight vehicle. More contemporary flight vehicles such as the Lockheed Martin F-22 Raptor are currently exhibiting nozzle degradation during normal operation and there is currently no known remedy.[8] This degradation is likely in part due to the loading induced by the engine exhaust.

Highly turbulent and heated jet plumes produced by rocket engines have significant effects on the launch pad structure and the airframe. The unsteady loading on the rocket airframe causes designers to carefully consider payload design to withstand structurally induced vibrations. Example predictions for noise induced rocket vibration were recently presented by Haynes and Kenny.[9] Their predictions relied heavily on empirical modeling and measurement data.

According to Green,[10] acoustic fatigue and subsequent failure of flight vehicles due to acoustic loading from jet plumes is an on-going problem in the aerospace industry. Howes et al.[11] showed that flight vehicle airframes near the jet plume undergo extremely high fluctuating pressures that induce structural fatigue and eventual failure. The lifetime of the flight vehicle is difficult to estimate with contemporary methods. Today, flight vehicle design must account for sonic fatigue due to jet fluid dynamics and associated aeroacoustics. The cross-correlation measurements of Howes et al.[11] in the jet near-field helped quantify these loads at various jet Mach numbers and temperature ratios. Unfortunately, there is no analytical approach to estimate these loadings or intensities. The calculation of these intensities and two-point statistics for airframe loading requires a model for the CPSD in the jet near-field. Acoustic loading calculations rely on the PSD and spatial coherent decay, thus the current validation effort is focused upon these two quantities.

The intention of this theoretically based investigation is to predict near-field CPSD from high speed heated compressible jets. Note that predicted near-field quantities are algebraically decaying and associated with acoustic propagation. This is in contrast with turbulent (hydrodynamic) quantities that are exponentially decaying. The model is based upon first principles and uses statistical quantities only when necessary. The essential features of the model are that it is in the form of an acoustic analogy, correctly predicts CPSD in the far-, mid-, and near-field for relevant jet Mach numbers and temperature ratios, incorporates the flight vehicle Mach number, and reduces to an auto-spectral model when both observers are at the same location. In the following sections we survey previous measurement and prediction efforts for two-point statistics of jet fluid physics and acoustics, develop the mathematical model, evaluate the model with measurement data in the far-, mid-, and near-field, and finally draw a conclusion.



S. A. E. Miller, Ph.D., s.miller@nasa.gov

### Survey of Previous Experiments and their Relation to the Present

The vast majority of investigations examining noise from jets are conducted by performing acoustic measurements at independent points. Statistics between observer positions is generally not considered. Conducting measurements at two or more points and subsequently examining two-point statistics allows for additional insight regarding the source of noise and the physics of jets. Maestrello,[12] motivated by a desire to gain additional insight into jet physics and radiated sound, conducted two-point measurements at NASA. Juve et al.[13] conducted a similar azimuthal correlation study of the far-field jet noise soon after. Maestrello[12] and Juve et al.[13] showed that coherence decays in the far-field with increasing observer angle separation and with increasing frequency.

Azimuthal modal decomposition was performed in the far-field using multiple acoustic arrays recently by Kopiev et al.[14] They quantified the azimuthal modal dependence of acoustic radiation relative to the axial source location. These significant findings were alluded to with the acoustic analogy approach of Ribner.[15] During the same year that Juve et al.[13] published their measurements, Bonnet and Fisher[16] examined ring source models, the resultant sound field, and resultant coherence. They argued that coherence in both the near- and far-field is mainly a function of frequency and is independent of any type of coherence of the structure within the noise source. This view is in contrast to that of Kopiev et al.[14] Predictions in this paper support both views of Juve et al.[13] and Kopiev et al.[14] in that turbulence contains both highly coherent and incoherent sources. The coherence depends on the radiation direction and radiation frequency.

Suzuki and Colonius[17] designed a near-field and mid-field concentric ring measurement array that completely surrounded the jet plume. These arrays were mounted in the Small Hot Jet Acoustic Rig (SHJAR) facility (see Bridges and Brown[18]) at NASA and a number of measurements were conducted with varying jet Mach number and temperature ratios. The SHJAR facility was also used by Lee and Bridges[19] with a far-field polar array that contained 16 microphones. Their measurements showed where the equivalent peak noise source location is as a function of frequency for the jet conditions studied by Suzuki and Colonius.[17] It was shown that the peak source location will approach the nozzle exit as the noise frequency under examination is increased.

Viswanathan[20] conducted the most comprehensive study to date, at the Low-Speed Aeroacoustic Facility of Boeing, for the variation of jet noise coherence. It can be observed that coherence as a function of frequency decays as a Gaussian function, transitions to a combination of Gaussian and exponentially decreasing functions, and finally an exponentially decaying function, as the separation between observer angles increases. Predictions in this paper show the same transition of coherence in the near-field and mid-field relative to measurements of Suzuki and Colonius[17] .

A number of array based measurements attempted to quantify the spatial distribution of the equivalent source. Some of the first approaches were by Billingsley and Kinns[21] and Fisher et al.[22] The later investigators created a method that quantified the equivalent source as a function of frequency in the jet streamwise direction. A more advanced source model is proposed in this paper and is inspired by Fisher et al.[22]

Perhaps a superior way to quantify the equivalent source is with direct measurement of the turbulent statistics within the jet plume. One recent study by Doty and McLaughlin[23] relied on an optical deflectometry system that did not disturb the flow-field while providing axially varying statistics within the jet plume. A similar study was performed by Panda and Seasholtz[24] who examined two-point statistics of fluctuating quantities using Rayleigh scattering. They examined two-point statistics of the various fluctuating quantities and also compared them with far-field radiating noise in the downstream direction. Panda and Mosher[25] examined rocket exhaust with a large 70 microphone array and derived contours of sound pressure level that illustrated the highly distributed source in a launch system environment. These particular studies are useful in the present work to help define the two-point cross-correlation of the Lighthill stress tensor.

### Survey of Previous Predictions and their Relation to the Present

Prediction of auto-spectra and cross-spectra mainly developed separately from the experimental investigations surveyed above. Countless investigators have applied computational fluid dynamics (CFD) approaches to predict jet auto-spectra. Some notable investigations include but are not limited to Shur et al.,[26] Mendez et al.,[27] Erwin et al.,[28] Uzun and Hussaini,[29] and Buhler et al.[30] These numerical simulations are very computationally expensive. Sound intensity levels often compare favorably with measurement but comparisons are usually performed for auto-spectra.

Another prediction approach is based on modeling instability waves within the jet and relating them to



S. A. E. Miller, Ph.D., s.miller@nasa.gov

the radiating field. Suzuki and Colonius[31] and Suzuki,[32] using the measured near-field and mid-field array data of Suzuki and Colonius,[17] conducted a series of studies that related wavepackets to the instability waves. In the former study, attention was paid to the relation between the instability waves and lower frequencies of jet noise. The latter study focused more on the noise source as modeled with the wavepacket approach. This paper relies heavily on the measurements conducted by Suzuki and Colonius.[17] Reba et al.[33] used two-point statistics of a near-field array close to various jets and projected sound to the mid-field using the wave equation. Cavalieri et al.[34] studied the velocity field of subsonic jets and discerned instability waves modeled as wavepackets. These wavepackets were connected to the radiated sound of the jet using measurements of the velocity field. Their study connected the wavepacket with the statistics of the jet flow and the acoustic intensity in the near-field.

A more analytical approach is based upon the acoustic analogy, which is an exact rearrangement of the governing equations of motion. Lighthill, in his now famous works on general theory[35] and turbulence as a source of sound,[36] introduced the acoustic analogy. Lighthill constructed a model for the equivalent source consisting of convecting quadrupoles that resulted in an estimate of jet noise intensity scaling as $M_j^8$, where $M_j$ is the fully expanded Mach number. This theory was revolutionary and predicted jet noise in the far-field. Lighthill's approach is the basis of the prediction method developed in this paper.

Perhaps the first serious acoustic analogy approach for the prediction of jet noise coherence (which is a function of CPSD) was performed by Ribner.[15] Ribner used the acoustic analogy approach of Lighthill[35] and formulated an expression for the coherence in the far-field about observers with equal distance to the nozzle exit. The theory relied on an isotropic turbulence assumption, non-compactness of the source region, and the directivity of the quadrupole equivalent source. The last assumption is responsible for the decay of coherence with increasing azimuthal observer angle. Ribner used a large body of excellent measurements by Maestrello[12] to validate his theory with relative success.

Richarz[37] extended the theory of Ribner[15] for the correlation between two observers in the jet far-field. Comparisons of coherence between far-field observers and measurement were satisfactory, but most importantly illustrated the need to model the source as non-compact even for jet far-field predictions. Harper-Bourne[38] developed semi-empirical prediction methods for the acoustic loading from the jet near-field on airframe structures. Semi-empirical methods were developed based on a spatially varying source specified by array measurements. The model consisted of two independent axial source functions. Comparison with measurements showed very good agreement but relied heavily on calibration data.

Using these previous investigations as guidance, we return to the original theory of Lighthill,[35] but with the goal of predicting near-field CPSD from high-speed heated compressible jets in the presence of a flight stream Mach number. Once we have obtained a general formulation, we construct a simple model for the jet source that is inspired by the work of Harper-Bourne.[38] An alternative source model based on steady Reynolds-averaged Navier-Stokes (RANS) solutions is developed in the appendix.

## Mathematical Theory

Here, we form a CPSD model for randomly fluctuating pressure near fluid turbulence in the presence of an ambient Mach number. The governing equations are the Navier-Stokes equations. We initially follow Lighthill[39] and define the continuity equation as

$$\frac{\partial \rho}{\partial t} + \frac{\partial \rho u_i}{\partial x_i} = 0 \tag{1}$$

and the momentum equation as

$$\frac{\partial \rho u_i}{\partial t} + \frac{\partial \rho u_i u_j}{\partial x_j} = \frac{\partial \tau_{ij}}{\partial x_j}, \tag{2}$$

where

$$\tau_{ij} = -p\delta_{ij} + \mu\left(\frac{\partial u_i}{\partial x_j} + \frac{\partial u_j}{\partial x_i}\right) - \frac{2}{3}\mu\frac{\partial u_k}{\partial x_k}\delta_{ij}, \tag{3}$$

$p$ is the pressure, $t$ is time, $\boldsymbol{u}$ is the velocity vector, $\boldsymbol{x}$ is the spatially independent variable, $\delta_{ij}$ is the Kronecker delta function, $\rho$ is the density, and $\mu$ is the viscosity. Terms where the same subscript resides imply summation (standard Einstein notation). We apply the partial derivative operator on Eqn. 1 with



S. A. E. Miller, Ph.D., s.miller@nasa.gov

respect to time and separately apply the divergence operator on Eqn. 2. Subtracting the modified continuity equation from the divergence of the momentum equation, then adding

$$\left(\frac{\partial^2 p}{\partial x_i \partial x_j} - c_\infty^2 \frac{\partial^2 \rho}{\partial x_i \partial x_j}\right) \delta_{ij} \tag{4}$$

to both sides of the resulting equation, and simplifying yields Lighthill's[35] acoustic analogy

$$\frac{\partial^2 \rho}{\partial t^2} - c_\infty^2 \frac{\partial^2 \rho}{\partial x_i \partial x_i} = \frac{\partial^2 T_{ij}}{\partial x_i \partial x_j}, \tag{5}$$

where $T_{ij}$ is the Lighthill stress tensor (see Lighthill[35] for details and discussion). We have now obtained a wave equation with a right hand side equivalent source. The Green's function of Eqn. 5 is governed by

$$\frac{\partial^2 g}{\partial t^2} - c_\infty^2 \frac{\partial^2 g}{\partial x_i \partial x_i} = \delta\left(\boldsymbol{x} - \boldsymbol{y}\right) \delta\left(t - \tau\right), \tag{6}$$

where $g(\boldsymbol{x}; \boldsymbol{y}, t; \tau)$ is the Green's function, $\boldsymbol{x}$ is an observer location, $\boldsymbol{y}$ is a source location, and $\delta$ is the Dirac delta function. It can easily be shown that the solution of Eqn. 6 in three-dimensional space is

$$g(\boldsymbol{x}; \boldsymbol{y}, t; \tau) = \frac{\delta\left(t - \tau - |\boldsymbol{x} - \boldsymbol{y}|/c_\infty\right)}{4\pi |\boldsymbol{x} - \boldsymbol{y}|}. \tag{7}$$

Using the Green's function and a convolution integral, the general solution of Eqn. 5 is

$$\rho - \rho_\infty = \frac{1}{4\pi c_\infty^2} \frac{\partial^2}{\partial x_i \partial x_j} \int_{-\infty}^{\infty} \int_{-\infty}^{\infty} \int_{-\infty}^{\infty} T_{ij}\left(\boldsymbol{y}, t - \frac{|\boldsymbol{x} - \boldsymbol{y}|}{c_\infty}\right) \frac{d\boldsymbol{y}}{|\boldsymbol{x} - \boldsymbol{y}|}. \tag{8}$$

Now that the general solution of the Lighthill acoustic analogy is obtained we pause and examine properties of differentiation with respect to the double divergence of $T_{ij}$. The integral of Eqn. 8 can be written after expanding $\partial/\partial x_j$

$$\begin{aligned} &\frac{\partial^2}{\partial x_i \partial x_j} \int_{-\infty}^{\infty} \int_{-\infty}^{\infty} \int_{-\infty}^{\infty} T_{ij}\left(\boldsymbol{y}, t - \frac{|\boldsymbol{x} - \boldsymbol{y}|}{c_\infty}\right) \frac{d\boldsymbol{y}}{|\boldsymbol{x} - \boldsymbol{y}|} \\ &= \underbrace{\frac{\partial}{\partial x_i} \int_{-\infty}^{\infty} \int_{-\infty}^{\infty} \int_{-\infty}^{\infty} \left\{ \frac{-(x_j - y_j)}{|\boldsymbol{x} - \boldsymbol{y}|} \frac{1}{|\boldsymbol{x} - \boldsymbol{y}|^2} T_{ij} \right\} d\boldsymbol{y}}_{\text{First Term}} \\ &+ \underbrace{\frac{\partial}{\partial x_i} \int_{-\infty}^{\infty} \int_{-\infty}^{\infty} \int_{-\infty}^{\infty} \left\{ \frac{-1}{c_\infty |\boldsymbol{x} - \boldsymbol{y}|} \frac{(x_j - y_j)}{|\boldsymbol{x} - \boldsymbol{y}|} \frac{\partial T_{ij}}{\partial t} \right\} d\boldsymbol{y}}_{\text{Second Term}}, \end{aligned} \tag{9}$$

where we have labeled the first and second term for convenience. Expanding the first term of Eqn. 9

$$\begin{aligned} \frac{\partial}{\partial x_i} \int_{-\infty}^{\infty} \int_{-\infty}^{\infty} \int_{-\infty}^{\infty} \left\{ \frac{-(x_j - y_j)}{|\boldsymbol{x} - \boldsymbol{y}|} \frac{1}{|\boldsymbol{x} - \boldsymbol{y}|^2} T_{ij} \right\} d\boldsymbol{y} = \int_{-\infty}^{\infty} \int_{-\infty}^{\infty} \int_{-\infty}^{\infty} \left\{ 3 \frac{(x_i - y_i)}{|\boldsymbol{x} - \boldsymbol{y}|} \frac{(x_j - y_j)}{|\boldsymbol{x} - \boldsymbol{y}|} \frac{T_{ij}}{|\boldsymbol{x} - \boldsymbol{y}|^3} \right. \\ \left. + \frac{(x_i - y_i)}{|\boldsymbol{x} - \boldsymbol{y}|} \frac{(x_j - y_j)}{|\boldsymbol{x} - \boldsymbol{y}|} \frac{1}{c_\infty |\boldsymbol{x} - \boldsymbol{y}|^2} \frac{\partial T_{ij}}{\partial t} - \delta_{ij} \frac{T_{ij}}{|\boldsymbol{x} - \boldsymbol{y}|^3} \right\} d\boldsymbol{y} \end{aligned} \tag{10}$$

and also expanding the second term of Eqn. 9

$$\begin{aligned} &\frac{\partial}{\partial x_i} \int_{-\infty}^{\infty} \int_{-\infty}^{\infty} \int_{-\infty}^{\infty} \left\{ \frac{1}{|\boldsymbol{x} - \boldsymbol{y}|} \frac{-1}{c_\infty} \frac{(x_j - y_j)}{|\boldsymbol{x} - \boldsymbol{y}|} \frac{\partial T_{ij}}{\partial t} \right\} d\boldsymbol{y} \\ &= \int_{-\infty}^{\infty} \int_{-\infty}^{\infty} \int_{-\infty}^{\infty} \left\{ 2 \frac{(x_i - y_i)}{|\boldsymbol{x} - \boldsymbol{y}|} \frac{(x_j - y_j)}{|\boldsymbol{x} - \boldsymbol{y}|} \frac{1}{c_\infty |\boldsymbol{x} - \boldsymbol{y}|^2} \frac{\partial T_{ij}}{\partial t} \right. \\ &\left. + \frac{(x_i - y_i)}{|\boldsymbol{x} - \boldsymbol{y}|} \frac{(x_j - y_j)}{|\boldsymbol{x} - \boldsymbol{y}|} \frac{1}{c_\infty^2 |\boldsymbol{x} - \boldsymbol{y}|^2} \frac{\partial^2 T_{ij}}{\partial t^2} - \delta_{ij} \frac{1}{c_\infty |\boldsymbol{x} - \boldsymbol{y}|^2} \frac{\partial T_{ij}}{\partial t} \right\} d\boldsymbol{y}. \end{aligned} \tag{11}$$



S. A. E. Miller, Ph.D., s.miller@nasa.gov

An excellent overview of this process is given by Lighthill,[35] but here we have retained all radiating terms. Using these expansions of the integrand, making substitutions for compactness, introducing a vector Mach number that convects the source (see Lighthill[35]), and converting to pressure, Eqn. 8 becomes

$$\begin{aligned} p\left(\boldsymbol{x},t\right) = \frac{1}{4\pi}\int_{-\infty}^{\infty}\int_{-\infty}^{\infty}\int_{-\infty}^{\infty}\Bigg\{ & \frac{r_i r_j}{r^2}\left[\frac{\ddot{T}_{ij}}{c_\infty^2 r}+\frac{3(1-M_\infty^2)\dot{T}_{ij}}{c_\infty r^2}+\frac{3(1-M_\infty^2)^2 T_{ij}}{r^3}\right] \\ & -\frac{2r_i M_{\infty,j}}{r}\left[\frac{2\dot{T}_{ij}}{c_\infty r^2}+\frac{3(1-M_\infty)^2 T_{ij}}{r^3}\right] \\ & -\delta_{ij}\left[\frac{\dot{T}_{ij}}{c_\infty r^2}+\frac{(1-M_\infty^2)T_{ij}}{r^3}\right] \\ & +2M_{\infty,i}M_{\infty,j}\frac{T_{ij}}{r^3}\Bigg\}\, d\boldsymbol{\eta}, \end{aligned} \tag{12}$$

where $r = |\boldsymbol{x}-\boldsymbol{y}| + \boldsymbol{M}_\infty\cdot(\boldsymbol{x}-\boldsymbol{y})$, $r_i = (x_i - y_i)\left(1+M_{\infty,i}\right)$, $\boldsymbol{y} = \boldsymbol{\eta} - c_\infty \boldsymbol{M}_\infty t + \boldsymbol{M}_\infty|\boldsymbol{x}-\boldsymbol{y}|$, and $\boldsymbol{M}_\infty$ is the vector free-stream Mach number. The vector $\boldsymbol{\eta} = \boldsymbol{\eta}(\xi,\eta,\zeta)$ is now the variable of integration over the source region. Arguments of the stress tensor are $T_{ij} = T_{ij}\left(\boldsymbol{\eta},\tau\right)$ and dot and double dot of $T_{ij}$ represent the first and second temporal derivatives, where $\tau = t - rc_\infty^{-1}$. Equation 12 represents the random pressure fluctuations as a function of observer time at observer $\boldsymbol{x}$. A second equation is written for random pressure fluctuations at observer $\boldsymbol{x}'$ and time $t'$

$$\begin{aligned} p\left(\boldsymbol{x}',t'\right) = \frac{1}{4\pi}\int_{-\infty}^{\infty}\int_{-\infty}^{\infty}\int_{-\infty}^{\infty}\Bigg\{ & \frac{r'_l r'_m}{r'^2}\left[\frac{\ddot{T}'_{lm}}{c_\infty^2 r'}+\frac{3(1-M_\infty^2)\dot{T}'_{lm}}{c_\infty r'^2}+\frac{3(1-M_\infty^2)^2 T'_{lm}}{r'^3}\right] \\ & -\frac{2r'_l M_{\infty,m}}{r'}\left[\frac{2\dot{T}'_{lm}}{c_\infty r'^2}+\frac{3(1-M_\infty)^2 T'_{lm}}{r'^3}\right] \\ & -\delta_{lm}\left[\frac{\dot{T}'_{lm}}{c_\infty r'^2}+\frac{(1-M_\infty^2)T'_{lm}}{r'^3}\right] \\ & +2M_{\infty,l}M_{\infty,m}\frac{T'_{lm}}{r'^3}\Bigg\}\, d\boldsymbol{\eta}', \end{aligned} \tag{13}$$

where the subscript $l$ and $m$ are analogous to $i$ and $j$.

Turbulence is a completely deterministic process, however, only statistical quantities of turbulent flow can be predicted. Thus, we are forced to pursue a statistical approach. We perform the two-point cross-correlation of Eqns. 12 and 13 and obtain

$$\overline{p\left(\boldsymbol{x},t\right)p\left(\boldsymbol{x}',t'\right)} = \frac{1}{16\pi^2}\int_{-\infty}^{\infty}\ldots\int_{-\infty}^{\infty}\left(A_1+A_2+A_3+A_4\right)d\boldsymbol{\eta}'d\boldsymbol{\eta}, \tag{14}$$

where '...' represents additional integrals and terms $A_1$ through $A_4$ are

$$\begin{aligned} A_1 = & \frac{r_i r_j r'_l r'_m}{r^2 r'^2}\overline{\left[\frac{\ddot{T}_{ij}}{c_\infty^2 r}+\frac{3(1-M_\infty^2)\dot{T}_{ij}}{c_\infty r^2}+\frac{3(1-M_\infty^2)^2 T_{ij}}{r^3}\right]\left[\frac{\ddot{T}'_{lm}}{c_\infty^2 r'}+\frac{3(1-M_\infty^2)\dot{T}'_{lm}}{c_\infty r'^2}+\frac{3(1-M_\infty^2)^2 T'_{lm}}{r'^3}\right]} \\ & -\frac{2r_i r_j}{rr}\frac{r'_l M_{\infty,m}}{r'}\overline{\left[\frac{\ddot{T}_{ij}}{c_\infty^2 r}+\frac{3(1-M_\infty^2)\dot{T}_{ij}}{c_\infty r^2}+\frac{3(1-M_\infty^2)^2 T_{ij}}{r^3}\right]\left[\frac{2\dot{T}'_{lm}}{c_\infty r'^2}+\frac{3(1-M_\infty)^2 T'_{lm}}{r'^3}\right]} \\ & -\frac{r_i r_j}{r^2}\delta_{lm}\overline{\left[\frac{\ddot{T}_{ij}}{c_\infty^2 r}+\frac{3(1-M_\infty^2)\dot{T}_{ij}}{c_\infty r^2}+\frac{3(1-M_\infty^2)^2 T_{ij}}{r^3}\right]\left[\frac{\dot{T}'_{lm}}{c_\infty r'^2}+\frac{(1-M_\infty^2)T'_{lm}}{r'^3}\right]} \\ & +\frac{2r_i r_j}{r^2}\frac{M_{\infty,l}M_{\infty,m}}{r'^3}\overline{\left[\frac{\ddot{T}_{ij}}{c_\infty^2 r}+\frac{3(1-M_\infty^2)\dot{T}_{ij}}{c_\infty r^2}+\frac{3(1-M_\infty^2)^2 T_{ij}}{r^3}\right]T'_{lm}}, \end{aligned} \tag{15}$$



S. A. E. Miller, Ph.D., s.miller@nasa.gov

$$
\begin{aligned}
A_2 = -\frac{2r_i M_{\infty,j}}{r}\frac{r'_l r'_m}{r'^2}\overline{\left[\frac{2\dot{T}_{ij}}{c_\infty r^2}+\frac{3(1-M_\infty)^2 T_{ij}}{r^3}\right]\left[\frac{\ddot{T}'_{lm}}{c_\infty^2 r'}+\frac{3(1-M_\infty^2)\dot{T}'_{lm}}{c_\infty r'^2}+\frac{3(1-M_\infty^2)^2 T'_{lm}}{r'^3}\right]} \\
+\frac{4r_i M_{\infty,j}}{r}\frac{r'_l M_{\infty,m}}{r'}\overline{\left[\frac{2\dot{T}_{ij}}{c_\infty r^2}+\frac{3(1-M_\infty)^2 T_{ij}}{r^3}\right]\left[\frac{2\dot{T}'_{lm}}{c_\infty r'^2}+\frac{3(1-M_\infty)^2 T'_{lm}}{r'^3}\right]} \\
+\frac{2r_i}{r}M_{\infty,j}\delta_{lm}\overline{\left[\frac{2\dot{T}_{ij}}{c_\infty r^2}+\frac{3(1-M_\infty)^2 T_{ij}}{r^3}\right]\left[\frac{\dot{T}'_{lm}}{c_\infty r'^2}+\frac{(1-M_\infty^2)T'_{lm}}{r'^3}\right]} \\
-\frac{4r_i M_{\infty,j}}{r}\frac{M_{\infty,l}M_{\infty,m}}{r'^3}\overline{\left[\frac{2\dot{T}_{ij}}{c_\infty r^2}+\frac{3(1-M_\infty)^2 T_{ij}}{r^3}\right]T'_{lm}},
\end{aligned}
\tag{16}
$$

$$
\begin{aligned}
A_3 = -\delta_{ij}\frac{r'_l r'_m}{r' r'}\overline{\left[\frac{\dot{T}_{ij}}{c_\infty r^2}+\frac{(1-M_\infty^2)T_{ij}}{r^3}\right]\left[\frac{\ddot{T}'_{lm}}{c_\infty^2 r'}+\frac{3(1-M_\infty^2)\dot{T}'_{lm}}{c_\infty r'^2}+\frac{3(1-M_\infty^2)^2 T'_{lm}}{r'^3}\right]} \\
+\delta_{ij}\frac{2r'_l M_{\infty,m}}{r'}\overline{\left[\frac{\dot{T}_{ij}}{c_\infty r^2}+\frac{(1-M_\infty^2)T_{ij}}{r^3}\right]\left[\frac{2\dot{T}'_{lm}}{c_\infty r'^2}+\frac{3(1-M_\infty)^2 T'_{lm}}{r'^3}\right]} \\
+\delta_{ij}\delta_{lm}\overline{\left[\frac{\dot{T}_{ij}}{c_\infty r^2}+\frac{(1-M_\infty^2)T_{ij}}{r^3}\right]\left[\frac{\dot{T}'_{lm}}{c_\infty r'^2}+\frac{(1-M_\infty^2)T'_{lm}}{r'^3}\right]} \\
-\delta_{ij}\frac{2M_{\infty,l}M_{\infty,m}}{r'^3}\overline{\left[\frac{\dot{T}_{ij}}{c_\infty r^2}+\frac{(1-M_\infty^2)T_{ij}}{r^3}\right]T'_{lm}},
\end{aligned}
\tag{17}
$$

and,

$$
\begin{aligned}
A_4 = \frac{2M_{\infty,i}M_{\infty,j}}{r^3}\frac{r'_l r'_m}{r' r'}\overline{T_{ij}\left[\frac{\ddot{T}'_{lm}}{c_\infty^2 r'}+\frac{3(1-M_\infty^2)\dot{T}'_{lm}}{c_\infty r'^2}+\frac{3(1-M_\infty^2)^2 T'_{lm}}{r'^3}\right]} \\
-\frac{4M_{\infty,i}M_{\infty,j}}{r^3}\frac{r'_l M_{\infty,m}}{r'}\overline{T_{ij}\left[\frac{2\dot{T}'_{lm}}{c_\infty r'^2}+\frac{3(1-M_\infty)^2 T'_{lm}}{r'^3}\right]} \\
-\delta_{lm}\frac{2M_{\infty,i}M_{\infty,j}}{r^3}\overline{T_{ij}\left[\frac{\dot{T}'_{lm}}{c_\infty r'^2}+\frac{(1-M_\infty^2)T'_{lm}}{r'^3}\right]} \\
+4\frac{M_{\infty,i}M_{\infty,j}}{r^3}\frac{M_{\infty,l}M_{\infty,m}}{r'^3}\overline{T_{ij}T'_{lm}}.
\end{aligned}
\tag{18}
$$

Note that in similar approaches the ambient speed of sound is removed from the integrand. This is not possible due to retaining the mid- and near-field terms. Equation 14 is very complicated and contains many different two-point cross-correlations of various combinations of quantities. Thus, we seek to simplify Eqn. 14. Detailed examinations of these two-point cross-correlations are shown by Lighthill,[39,35] Ribner,[15] and Ffowcs Williams.[40] We note that $\overline{\dot{T}_{ij}T'_{lm}}=0$ and $\overline{\ddot{T}_{ij}T'_{lm}}=-\overline{\dot{T}_{ij}\dot{T}'_{lm}}$ are assumed to be statistically stationary random functions in time (discussed by Ribner[15]). These simplifications are used in conjunction with Eqn. 14. We then group integrand terms according to their relative contribution to the near-field, mid-field, and far-field. Terms with second order powers in propagation correspond to far-field terms, fourth order powers correspond to the mid-field terms, and sixth order powers correspond to near-field terms. These operations result in

$$
\overline{p\left(\boldsymbol{x},t\right)p\left(\boldsymbol{x}',t'\right)}=\frac{1}{16\pi^2}\int_{-\infty}^{\infty}\ldots\int_{-\infty}^{\infty}F_t\overline{\ddot{T}_{ij}\ddot{T}'_{lm}}+M_t\overline{\dot{T}_{ij}\dot{T}'_{lm}}+N_t\overline{T_{ij}T'_{lm}}d\boldsymbol{\eta}'d\boldsymbol{\eta},
\tag{19}
$$

where the far-field term is

$$
F_t=\frac{r_i r_j r'_l r'_m}{r^2 r'^2}\left[\frac{1}{c_\infty^4 r r'}\right],
\tag{20}
$$



S. A. E. Miller, Ph.D., s.miller@nasa.gov

the mid-field term is

$$
\begin{aligned}
M_t = &\frac{r_i r_j r'_l r'_m}{r^2 r'^2}\left[\frac{9(1-M_\infty^2)^2}{c_\infty^2 r^2 r'^2} - \frac{3(1-M_\infty^2)^2}{c_\infty^2 r r'^3} - \frac{3(1-M_\infty^2)^2}{c_\infty^2 r^3 r'}\right] \\
&- \frac{r_i r_j r'_l}{r^2 r'}\left[\frac{6(1-M_\infty^2)}{c_\infty^2}\left(\frac{2M_{\infty,m}}{r^2 r'^2} - \frac{M_{\infty,m}}{r r'^3}\right)\right] - \frac{r_i r'_l r'_m}{r r'^2}\left[\frac{6(1-M_\infty^2)}{c_\infty^2}\left(\frac{2M_{\infty,j}}{r^2 r'^2} - \frac{M_{\infty,j}}{r^3 r'}\right)\right] \\
&- \frac{r_i r_j}{r^2}\left[\frac{3(1-M_\infty^2)\delta_{lm}}{c_\infty^2 r^2 r'^2} + \frac{(1-M_\infty^2)\delta_{lm}}{c_\infty^2 r r'^3} + \frac{2M_{\infty,l}M_{\infty,m}}{c_\infty^2 r r'^3}\right] \\
&- \frac{r'_l r'_m}{r'^2}\left[\frac{3(1-M_\infty^2)\delta_{ij}}{c_\infty^2 r^2 r'^2} + \frac{(1-M_\infty^2)\delta_{ij}}{c_\infty^2 r^3 r'} + \frac{2M_{\infty,i}M_{\infty,j}}{c_\infty^2 r^3 r'}\right] \\
&+ \frac{r_i r'_l}{r r'}\left[\frac{16M_{\infty,j}M_{\infty,m}}{c_\infty^2 r^2 r'^2}\right] + \frac{r_i}{r}\left[\frac{4M_{\infty,j}\delta_{lm}}{c_\infty^2 r^2 r'^2}\right] + \frac{r'_l}{r'}\left[\frac{4M_{\infty,m}\delta_{ij}}{c_\infty^2 r^2 r'^2}\right] + \frac{\delta_{ij}\delta_{lm}}{c_\infty^2 r^2 r'^2},
\end{aligned}
\tag{21}
$$

and the near-field term is

$$
\begin{aligned}
N_t = &\frac{r_i r_j r'_l r'_m}{r^2 r'^2}\left[\frac{9(1-M_\infty^2)^4}{r^3 r'^3}\right] - \frac{r_i r_j r'_l}{r^2 r'}\left[\frac{18M_{\infty,m}(1-M_\infty^2)^2(1-M_\infty)^2}{r^3 r'^3}\right] \\
&- \frac{r_i r'_l r'_m}{r r'^2}\left[\frac{18M_{\infty,j}(1-M_\infty^2)^2(1-M_\infty)^2}{r^3 r'^3}\right] + \frac{r_i r_j}{r^2}\left[\frac{3(1-M_\infty^2)^2}{r^3 r'^3}\left(2M_{\infty,l}M_{\infty,m} - (1-M_\infty^2)\delta_{lm}\right)\right] \\
&+ \frac{r'_l r'_m}{r'^2}\left[\frac{3(1-M_\infty^2)^2}{r^3 r'^3}\left(2M_{\infty,i}M_{\infty,j} - (1-M_\infty^2)\delta_{ij}\right)\right] + \frac{r_i r'_l}{r r'}\left[\frac{36M_{\infty,j}M_{\infty,m}(1-M_\infty)^4}{r^3 r'^3}\right] \\
&- \frac{r_i}{r}\left[\frac{6(1-M_\infty)^2 M_{\infty,j}}{r^3 r'^3}\left(2M_{\infty,l}M_{\infty,m} - (1-M_\infty^2)\delta_{lm}\right)\right] \\
&- \frac{r'_l}{r'}\left[\frac{6(1-M_\infty)^2 M_{\infty,m}}{r^3 r'^3}\left(2M_{\infty,i}M_{\infty,j} - (1-M_\infty^2)\delta_{ij}\right)\right] \\
&-2(1-M_\infty^2)\left[\frac{M_{\infty,i}M_{\infty,j}\delta_{lm}}{r^3 r'^3} + \frac{M_{\infty,l}M_{\infty,m}\delta_{ij}}{r^3 r'^3}\right] + \frac{4M_{\infty,i}M_{\infty,j}M_{\infty,l}M_{\infty,m}}{r^3 r'^3} + \frac{(1-M_\infty^2)^2\delta_{ij}\delta_{lm}}{r^3 r'^3}.
\end{aligned}
\tag{22}
$$

The terms in Eqns. 20 through 22 have been grouped by descending order of effective trigonomic angles of the observer vector. If the vector ambient Mach number, $\boldsymbol{M}_\infty = 0$, then Eqn. 19 is relatively compact

$$
\begin{aligned}
\overline{p(\boldsymbol{x},t)\,p(\boldsymbol{x}',t')} = &\frac{1}{16\pi^2}\int_{-\infty}^{\infty}\cdots\int_{-\infty}^{\infty}\left\{\left\{\frac{r_i r_j r'_l r'_m}{r^2 r'^2}\right\}\frac{\overline{\ddot{T}_{ij}\ddot{T}'_{lm}}}{c_\infty^4 r r'}\right. \\
&+\left\{\frac{r_i r_j r'_l r'_m}{r^2 r'^2}\left[\frac{9}{c_\infty^2 r^2 r'^2} - \frac{3}{c_\infty^2 r r'^3} - \frac{3}{c_\infty^2 r^3 r'}\right] - \frac{r_i r_j}{r^2}\left[\frac{3\delta_{lm}}{c_\infty^2 r^2 r'^2} + \frac{\delta_{lm}}{c_\infty^2 r r'^3}\right]\right. \\
&\left.\left. - \frac{r'_l r'_m}{r'^2}\left[\frac{3\delta_{ij}}{c_\infty^2 r^2 r'^2} + \frac{\delta_{ij}}{c_\infty^2 r^3 r'}\right] + \frac{\delta_{ij}\delta_{lm}}{c_\infty^2 r^2 r'^2}\right\}\overline{\dot{T}_{ij}\dot{T}'_{lm}}\right. \\
&\left.+\left\{\frac{r_i r_j r'_l r'_m}{r^2 r'^2}\left[\frac{9}{r^3 r'^3}\right] - \frac{r_i r_j}{r^2}\left[\frac{3\delta_{lm}}{r^3 r'^3}\right] - \frac{r'_l r'_m}{r'^2}\left[\frac{3\delta_{ij}}{r^3 r'^3}\right] + \frac{\delta_{ij}\delta_{lm}}{r^3 r'^3}\right\}\overline{T_{ij}T'_{lm}}\right\} d\boldsymbol{\eta}' d\boldsymbol{\eta}.
\end{aligned}
\tag{23}
$$

We define the CPSD as

$$
G(\boldsymbol{x}_1,\boldsymbol{x}_2,\omega) = \int_{-\infty}^{\infty}\overline{p(\boldsymbol{x}_1,t)\,p(\boldsymbol{x}_2,t+\tau)}\exp\left[-i\omega\left(\tau + \frac{r_1}{c_\infty} - \frac{r_2}{c_\infty}\right)\right]d\tau,
\tag{24}
$$

where $t' = t+\tau$ and subscripts 1 and 2 represent two separate positions. Note here that $r_1$ and $r_2$ are vector magnitudes and not components. Particularly astute readers will note that volumetric integration over a source region when $\boldsymbol{x} = \boldsymbol{x}_1 = \boldsymbol{x}_2$ will yield a real quantity and $G(\boldsymbol{x}_1,\boldsymbol{x}_2,\omega)$ will reduce to the auto-power spectral density $S(\boldsymbol{x},\omega)$. Substituting Eqn. 19 into Eqn. 24 yields



S. A. E. Miller, Ph.D., s.miller@nasa.gov

$$G\left(\boldsymbol{x}_1,\boldsymbol{x}_2,\omega\right)=\frac{1}{16\pi^2}\int_{-\infty}^{\infty}...\int_{-\infty}^{\infty}\left\{\overbrace{F_t\overline{\ddot{T}_{ij}\ddot{T}'_{lm}}}^{\text{Far-Field Term}}+\overbrace{M_t\overline{\dot{T}_{ij}\dot{T}'_{lm}}}^{\text{Mid-Field Term}}+\overbrace{N_t\overline{T_{ij}T'_{lm}}}^{\text{Near-Field Term}}\right\}\times\exp\left[-i\omega\left(\tau+\frac{r_1}{c_\infty}-\frac{r_2}{c_\infty}\right)\right]d\tau d\boldsymbol{\eta}' d\boldsymbol{\eta}. \tag{25}$$

Equation 25 is the CPSD due to a convecting turbulent field within a free-stream Mach number. Its application is not limited to jets. The three terms within the integrand, 'Far-Field,' 'Mid-Field,' and 'Near-Field' are grouped based upon the inverse power of propagation distance. It will be shown below that these terms relative contributions to the intensity at $\boldsymbol{x}$ are not necessarily restricted to radiation distance. To evaluate Eqn. 25 knowledge of $\overline{T_{ij}T'_{lm}}$ and its derivatives must be known. These quantities can be calculated numerically using unsteady CFD. We construct a model for $\overline{T_{ij}T'_{lm}}$ and propose a second model based on steady RANS solutions in the appendix.

### The Variation of $F_t$, $M_t$, and $N_t$ with Radial Position and Free-Stream Mach Number

Before we turn to the task of creating a model for $\overline{T_{ij}T'_{lm}}$, we examine the variation of $F_t$, $M_t$, and $N_t$ with varying radial position and free-stream Mach number. The derivation of the far-field, mid-field, and near-field terms shown in Eqns. 20 through 22 respectively illustrate the fall-off of the intensity relative to the turbulent source. The spectral density decays as $r^{-2}$, $r^{-4}$, and $r^{-6}$ for the $F_t$, $M_t$, and $N_t$ terms respectively. These three pre-factor terms are functions of observer positions and the free-stream Mach number. To illustrate their relative magnitude and decay in the most basic fashion, we restrict $x_1 = x_2$, vary the observer position in the plane of the nozzle exit from one to one hundred nozzle diameters away from the nozzle exit, and vary the free-stream Mach number from zero to one half. Figures 1(a) through 1(c) show contour plots of $F_t$, $M_t$, and $N_t$ respectively. The $y$-axis is the magnitude of $M_\infty$ and is orthogonal to the radial observer location, and the $x$-axis is the logarithm of the radial position normalized by the nozzle exit diameter. Large variation in magnitude is observed between the three terms and is mainly attributed to the ambient speed of sound factors present in the denominator. Note there is no variation in $F_t$ with increasing $M_\infty$ at this radiation angle because $M_\infty$ does not appear in the term explicitly, and the dot product of the observer vector with $\boldsymbol{M}_\infty$ is zero. At radiation angles other than the sideline and $M_\infty > 0$, the variation of the $F_t$ term will be dependent on $\boldsymbol{M}_\infty$.

### Modeling the Two-Point Cross-Correlation of the Lighthill Stress Tensor

In this section, we seek models of $\overline{\ddot{T}_{ij}\ddot{T}'_{lm}}$, $\overline{\dot{T}_{ij}\dot{T}'_{lm}}$, and $\overline{T_{ij}T'_{lm}}$. We assume that the first two two-point cross-correlations involving derivatives are dependent on the latter. Detailed examinations of these two-point cross-correlations are shown by Lighthill,[39,35] Ribner,[15] and Ffowcs Williams.[40] For simplicity, we define the two-point cross-correlation of the Lighthill stress tensor as

$$\overline{T_{ij}T'_{lm}}=R_{ijlm}(\boldsymbol{y}_1,\boldsymbol{\eta},\tau), \tag{26}$$

where $\boldsymbol{\eta}=\boldsymbol{\eta}(\xi,\eta,\zeta)$ is a vector between source positions $\boldsymbol{y}_1$ and $\boldsymbol{y}_2$. Goldstein[41] showed that cross-correlations involving derivatives of the same order can be written

$$\overline{\frac{\partial^2}{\partial\tau^2}T_{ij}\frac{\partial^2}{\partial\tau^2}T'_{lm}}=\frac{\partial^4}{\partial\tau^4}R_{ijlm}(\boldsymbol{y}_1,\boldsymbol{\eta},\tau) \tag{27}$$

and similarily it can be shown

$$\overline{\frac{\partial}{\partial\tau}T_{ij}\frac{\partial}{\partial\tau}T'_{lm}}=\frac{\partial^2}{\partial\tau^2}R_{ijlm}(\boldsymbol{y}_1,\boldsymbol{\eta},\tau). \tag{28}$$

This approach was used and justified by Ribner.[15] We propose a model for the two-point cross-correlation of the Lighthill stress tensor

$$\overline{T_{ij}T'_{lm}}=\frac{A_{ijlm}}{\pi^{1/2}}\exp\left[\frac{-|\xi|}{\overline{u}\tau_s}\right]\exp\left[\frac{-(\xi-\overline{u}\tau)^2}{l_s^2}\right]\exp\left[\frac{-\eta^2}{l_{sy}^2}\right]\exp\left[\frac{-\zeta^2}{l_{sz}^2}\right], \tag{29}$$



S. A. E. Miller, Ph.D., s.miller@nasa.gov

where $A_{ijlm}$ is a coefficient that must be modeled based on local flow quantities within the plume, $l_s$ is the streamwise turbulent length scale, $l_{sy}$ and $l_{sz}$ are the cross-stream turbulent length scales, $\overline{u}$ is the effective axial velocity at $\boldsymbol{y}$, and $\tau_s$ is the turbulent time scale. Though the model will not capture characteristic 'negative loops' observed in measurement, the proposed model is consistent with Tam.[42] Morris and Farassat,[43] and Miller[44] also demonstrated accurate predictions relative to measurement using this model. The selection of this model also allows the derivatives and integrals with respect to time and space to be performed analytically and yields appropriate powers of $\omega$ that are consistent with Tam,[42] Morris and Farassat[43] and Miller.[44] Furthermore, by choosing to use the coefficient matrix $A_{ijlm}$, the potential to include anisotropic effects of turbulence is possible. Inclusion of these effects can be beneficial as shown by Khavaran.[45]

Substituting Eqn. 29 into Eqn. 27 and performing the fourth order derivative with respect to $\tau$ yields

$$\begin{aligned}\frac{\partial^4}{\partial\tau^4}R_{ijlm}(\boldsymbol{y}_1,\boldsymbol{\eta},\tau) = \frac{4A_{ijlm}\overline{u}^4}{\pi^{1/2}l_s^8}\left(3l_s^4 - 12l_s^2(\xi-\overline{u}\tau)^2 + 4(\xi-\overline{u}\tau)^4\right)\\ \times\exp\left[\frac{-|\xi|}{\overline{u}\tau_s}\right]\exp\left[\frac{-(\xi-\overline{u}\tau)^2}{l_s^2}\right]\exp\left[\frac{-\eta^2}{l_{sy}^2}\right]\exp\left[\frac{-\zeta^2}{l_{sz}^2}\right].\end{aligned} \tag{30}$$

Similarly, substituting Eqn. 29 into Eqn. 28 and performing the second order derivative with respect to $\tau$ yields

$$\begin{aligned}\frac{\partial^2}{\partial\tau^2}R_{ijlm}(\boldsymbol{y}_1,\boldsymbol{\eta},\tau) = \frac{2A_{ijlm}\overline{u}^2}{\pi^{1/2}l_s^4}\left(l_s^2 - 2(\xi-\overline{u}\tau)^2\right)\\ \times\exp\left[\frac{-|\xi|}{\overline{u}\tau_s}\right]\exp\left[\frac{-(\xi-\overline{u}\tau)^2}{l_s^2}\right]\exp\left[\frac{-\eta^2}{l_{sy}^2}\right]\exp\left[\frac{-\zeta^2}{l_{sz}^2}\right].\end{aligned} \tag{31}$$

Multiplying Eqn. 30 by $\exp\left[-i\omega\tau - i\omega r/c_\infty + i\omega r'/c_\infty\right]$ and integrating with respect to $\tau$ yields

$$\begin{aligned}&\int_{-\infty}^{\infty}\frac{\partial^4}{\partial\tau^4}\left[R_{ijlm}(\boldsymbol{y}_1,\boldsymbol{\eta},\tau)\right]\exp\left[-i\omega\left(\tau + \frac{|\boldsymbol{x}_1-\boldsymbol{y}_1|}{c_\infty} - \frac{|\boldsymbol{x}_2-\boldsymbol{y}_2|}{c_\infty}\right)\right]d\tau\\ &= A_{ijlm}\frac{l_s\omega^4}{\overline{u}}\exp\left[\frac{-i\xi\omega}{\overline{u}}\right]\exp\left[\frac{-|\xi|}{\overline{u}\tau_s}\right]\exp\left[\frac{-\eta^2}{l_{sy}^2}\right]\exp\left[\frac{-\zeta^2}{l_{sz}^2}\right]\exp\left[\frac{-l_s^2\omega^2}{4\overline{u}^2}\right]\exp\left[\frac{-i\omega(r-r')}{c_\infty}\right].\end{aligned} \tag{32}$$

Similarly, multiplying Eqns. 31 and 26 by $\exp\left[-i\omega\tau - i\omega r/c_\infty + i\omega r'/c_\infty\right]$ respectively and integrating with respect to $\tau$ yields

$$\begin{aligned}&\int_{-\infty}^{\infty}\frac{\partial^2}{\partial\tau^2}\left[R_{ijlm}(\boldsymbol{y}_1,\boldsymbol{\eta},\tau)\right]\exp\left[-i\omega\left(\tau + \frac{|\boldsymbol{x}_1-\boldsymbol{y}_1|}{c_\infty} - \frac{|\boldsymbol{x}_2-\boldsymbol{y}_2|}{c_\infty}\right)\right]d\tau\\ &= \frac{A_{ijlm}l_s\omega^2}{\overline{u}}\exp\left[\frac{-i\xi\omega}{\overline{u}}\right]\exp\left[\frac{-|\xi|}{\overline{u}\tau_s}\right]\exp\left[\frac{-\eta^2}{l_{sy}^2}\right]\exp\left[\frac{-\zeta^2}{l_{sz}^2}\right]\exp\left[\frac{-l_s^2\omega^2}{4\overline{u}^2}\right]\exp\left[\frac{-i\omega(r-r')}{c_\infty}\right]\end{aligned} \tag{33}$$

and

$$\begin{aligned}&\int_{-\infty}^{\infty}R_{ijlm}(\boldsymbol{y}_1,\boldsymbol{\eta},\tau)\exp\left[-i\omega\left(\tau + \frac{|\boldsymbol{x}_1-\boldsymbol{y}_1|}{c_\infty} - \frac{|\boldsymbol{x}_2-\boldsymbol{y}_2|}{c_\infty}\right)\right]d\tau\\ &= \frac{A_{ijlm}l_s}{\overline{u}}\exp\left[\frac{-i\xi\omega}{\overline{u}}\right]\exp\left[\frac{-|\xi|}{\overline{u}\tau_s}\right]\exp\left[\frac{-\eta^2}{l_{sy}^2}\right]\exp\left[\frac{-\zeta^2}{l_{sz}^2}\right]\exp\left[\frac{-l_s^2\omega^2}{4\overline{u}^2}\right]\exp\left[\frac{-i\omega(r-r')}{c_\infty}\right],\end{aligned} \tag{34}$$

respectively.

Equations 26 through 29 and 32 through 34 are substituted into Eqn. 25 giving

$$\begin{aligned}G\left(\boldsymbol{x}_1,\boldsymbol{x}_2,\omega\right) = \frac{1}{16\pi^2}\int_{-\infty}^{\infty}\ldots\int_{-\infty}^{\infty}\frac{A_{ijlm}l_s}{\overline{u}}\left\{F_t\omega^4 + M_t\omega^2 + N_t\right\}\\ \times\exp\left[\frac{-i\xi\omega}{\overline{u}}\right]\exp\left[\frac{-|\xi|}{\overline{u}\tau_s}\right]\exp\left[\frac{-\eta^2}{l_{sy}^2}\right]\exp\left[\frac{-\zeta^2}{l_{sz}^2}\right]\exp\left[\frac{-l_s^2\omega^2}{4\overline{u}^2}\right]\exp\left[\frac{-i\omega(r-r')}{c_\infty}\right]d\boldsymbol{\eta}'d\boldsymbol{\eta}.\end{aligned} \tag{35}$$

Terms in Eqn. 35 can now be modeled using steady RANS solutions as shown in the appendix. Some readers may be concerned about the term, $\overline{u}$, in the denominator of the resulting integrations. The integration



S. A. E. Miller, Ph.D., s.miller@nasa.gov

over $\xi$ from $-\infty$ to $\infty$, which is often performed for far-field auto-correlation models, results in a term with $\overline{u}$ in the numerator. Thus, even with localized $\overline{u} = 0$ within a turbulent flow, the singularity will not occur when Eqn. 35 is evaluated. The possibility of having a singularity due to a streamwise meanflow velocity of zero is not possible in the application of the model.

### An Effective Anisotropic Model

Here, we form a relatively simple model for the stochastic terms of Eqn. 35. We assume that these stochastic terms can be represented as effective overall values and are strongly dependent on the axial location within the jet. Using this assumption, the effective properties' dependence on $\eta$ and $\zeta$ are minimal. The cross-stream integrals are

$$\int_{-\infty}^{\infty} \exp\left[\frac{-\eta'^2}{l_{sy}^2}\right] d\eta' = \pi^{1/2} l_{sy} \tag{36}$$

and similarly

$$\int_{-\infty}^{\infty} \exp\left[\frac{-\zeta'^2}{l_{sz}^2}\right] d\zeta' = \pi^{1/2} l_{sz}. \tag{37}$$

Thus, Eqn. 35 can be written

$$\begin{aligned} G\left(\boldsymbol{x}_1, \boldsymbol{x}_2, \omega\right) = \frac{1}{16\pi} \int_{-\infty}^{\infty} ... \int_{-\infty}^{\infty} \left\{ \frac{A_{ijlm} l_s l_{sy} l_{sz}}{\overline{u}} \left\{ F_t \omega^4 + M_t \omega^2 + N_t \right\} \right. \\ \left. \times \exp\left[\frac{-i\xi\omega}{\overline{u}}\right] \exp\left[\frac{-|\xi|}{\overline{u}\tau_s}\right] \exp\left[\frac{-l_s^2\omega^2}{4\overline{u}^2}\right] \exp\left[\frac{-i\omega(r-r')}{c_\infty}\right] \right\} d\xi' d\boldsymbol{\eta}. \end{aligned} \tag{38}$$

The term $A_{ijlm}$ represents coefficients of the fourth order two-point cross-correlation of the stress tensor. We propose a model for $A_{ijlm}$

$$\begin{aligned} A_{ijlm} = P_f A_{ij} A_{lm} S_y \exp\left[ -\frac{10}{3} St^{1/2} \left\{ \left| \arg\left[r_3 + ir_2\right] - \arg\left[r_3' + ir_2'\right] \right| \right. \right. \\ \left. \left. + \left| \arg\left[\left(r_2 + r_3\right)^{1/2} + ir_1\right] - \arg\left[\left(r_2' + r_3'\right)^{1/2} + ir_1'\right] \right|^2 \right\} \right], \end{aligned} \tag{39}$$

where $P_f = \pi(10^{-17/5})^2$ is a constant, arg is the argument, and the other terms are described below. Prediction of the coherence in the near-field does exhibit decay with increasing frequency and separation angle between observers. However, the decay is sometimes too weak without the exponential term. Thus, the term involving arguments of observer position and frequency is proposed in Eqn. 39. The arguments of angles in Eqn. 39 are dependent on observer position and weakly on frequency. The latter term is equivalent to the natural property of turbulence radiating sound; that is sound becomes less coherent relative to increasing frequency and increasing radiation angle. Anisotropy of $A_{ijlm}$ is incorporated by setting the coefficients of $A_{ij}$ and $A_{lm}$ as

$$A_{ij} = \sigma^{1/2} \begin{bmatrix} a_{11} & \frac{1}{3} & \frac{1}{3} \\ \frac{1}{3} & 1 & \frac{1}{3} \\ \frac{1}{3} & \frac{1}{3} & 1 \end{bmatrix} \quad \text{and} \quad A_{lm} = \sigma^{1/2} \begin{bmatrix} b_{11} & \frac{1}{3} & \frac{1}{3} \\ \frac{1}{3} & 1 & \frac{1}{3} \\ \frac{1}{3} & \frac{1}{3} & 1 \end{bmatrix}, \tag{40}$$

where $\sigma$ is a function that is dependent on the Mach number and frequency of the acoustic radiation

$$\sigma = \exp\left[ -\left( \ln[St] - \ln\left[\frac{7}{100} + \frac{13}{100}(1 - M_j)\right]\right)^2 \left(1 + \frac{3}{5}\left(M_j - 1\right)\right) \sigma_f^4 \right] \tag{41}$$

and $\sigma_f$ is

$$\sigma_f = \begin{cases} \frac{((1-M_cM_j)^2 + (\beta_s M_c M_j)^2)^{1/2}}{((1-M_cM_j r_1/r)^2 + (\beta_s M_c M_j)^2)^{1/2}} & \text{if } M_c M_j < 1 \\ \frac{\beta_s M_c M_j}{((1-M_cM_j r_1/r)^2 + (\beta_s M_c M_j)^2)^{1/2}} & \text{if } M_c M_j \geq 1. \end{cases} \tag{42}$$



S. A. E. Miller, Ph.D., s.miller@nasa.gov

The first coefficients of $A_{ij}$ and $A_{lm}$ are

$$a_{11} = \left( \frac{\left\{1 + (\beta_s M_c M_j)^2\right\}^{1/2}}{\left\{(1 - M_c M_j r_1/r)^2 + (\beta_s M_c M_j)^2\right\}^{1/2}} \right)^{5/2} \tag{43}$$

and

$$b_{11} = \left( \frac{\left\{1 + (\beta_s M_c M_j)^2\right\}^{1/2}}{\left\{(1 - M_c M_j r_1'/r')^2 + (\beta_s M_c M_j)^2\right\}^{1/2}} \right)^{5/2}, \tag{44}$$

where $M_c = 0.70$ is a constant coefficient that represents the overall fraction of the effective convective Mach number and $\beta_s = 10^{-1}$ is a constant. The form of the coefficients, $a_{11}$ and $b_{11}$, and their powers are chosen based on the model of Ffowcs Williams.[40] If $\boldsymbol{x}_1 = \boldsymbol{x}_2$ and $x \gg y$, then the coefficients effectively have a fifth power. The equivalent spatial source distribution is modeled by the term $S_y$ in Eqn. 39 as

$$S_y = k_{max}^2 \overline{\rho}^2 \left(1 + \frac{St^{-3}}{200}\right) \exp\left[-\frac{5}{2} \ln\left[\frac{y_1 D_j St^{1/10}}{y_c}\right]^2\right], \tag{45}$$

where $k_{\max}$ is the maximum effective turbulent kinetic energy in the jet plume. Extensive numerical simulations suggest that $k_{\max}$ is approximately

$$k_{max} = k_f M_j^{5/2} \mathrm{TTR}^{Pr + Pr_t\left(1 - \mathrm{erf}\left[2M_j^2\right]\right)}, \tag{46}$$

where Erf is the error function, $k_f = 3 \times 10^3$ is a constant, $Pr = 0.72$ is the Prandtl number, and $Pr_t = 0.90$ is the turbulent Prandtl number. The total temperature ratio (TTR) is the plenum stagnation temperature divided by the ambient static temperature. Figure 2 shows a comparison of predicted $k_{max}$ using Eqn. 46 with $k_{max}$ extracted from steady RANS solutions.

Equation 38 contains turbulent length and time scales. We approximate the turbulent length scale as

$$l_s = \alpha_l \left(0.1028 M_j + 0.0654\right) y_1 D_j, \tag{47}$$

where $\alpha_l = 1.07$ is the spreading rate per unit $D_j$. Equation 47 is created based on the same steady RANS solutions that Eqn. 46 is based upon, and it yields slopes of increasing integral length scale with increasing axial distance from the nozzle exit. Equation 47 has similar agreement with length scales derived from steady RANS. The cross-stream turbulent length scales, $l_{sy}$ and $l_{sz}$, are one-third of $l_s$. The turbulent time scale is a function of the local turbulent length scale, $\tau_s = l_s/\overline{u}$.

The spatially varying time-averaged stream-wise velocity component and temperature proposed here are approximated using the models of Lau et al.[46] and Lau,[47] and these have been modified to incorporate the free-stream Mach number. The effective streamwise velocity component is

$$\overline{u} = \begin{cases} u_j & \text{if } y_1 < y_c \\ \left(u_j - u_\infty\right)\left(1 - \exp\left[\frac{1.35}{1 - y_1/y_c}\right]\right) + u_\infty & \text{if } y_1 \geq y_c \end{cases} \tag{48}$$

and similarly for $\overline{T}$

$$\overline{T} = \begin{cases} T_j & \text{if } y_1 < y_c \\ \left(T_j - T_\infty\right)\left(1 - \exp\left[\frac{1.35}{1 - y_1/y_c}\right]\right) + T_\infty & \text{if } y_1 \geq y_c, \end{cases} \tag{49}$$

where $y_c$ is the jet core length. The core length is estimated using the model of Tam.[48] The core length $y_c$ is

$$y_c = \begin{cases} D_j\left(4.3 + 1.2M_j^2 + 1.2(1 - T_j/T_\infty)\right) & \text{if } T_j < T_\infty \\ D_j\left(4.3 + 1.2M_j^2\right) & \text{if } T_j \geq T_\infty. \end{cases} \tag{50}$$

A better approximation would model $\overline{u}$ and $\overline{T}$ as effective equivalent radially averaged properties instead of local centerline averaged quantities. This investigation is focused on turbulent mixing and we assume

$\overline{p} \approx p_\infty$ throughout the jet plume. The density varies as, $\overline{\rho} = \overline{p} R_g^{-1} \overline{T}^{-1}$, and the speed of sound as, $\overline{c} = (\gamma R_g \overline{T})^{1/2}$. Finally, the effective axial Mach number is, $\overline{M} = \overline{u}(\gamma R_g \overline{T})^{-1/2}$.

### Equivalent Source Comparisons with Measurement

We pause here to examine the developed source model present within Eqns. 38 and 39. Figure 3 shows comparisons between the developed equivalent source model, the predictions of Tam et al.,[49] and the experiments of Schlinker[50] and Laufer et al.[51] We follow the approach of Tam et al.[49] by plotting the relative strength on the $y$-axis and the axial location, $x/D$, on the $x$-axis. Relative source strength is normalized by the maximum strength per prediction or measurement. All predictions and measurements are at the sideline observer location (following the validation approach of Tam et al.[49]). Figure 3(a) shows the equivalent source strength per unit length of the developed approach as a solid line, the prediction of Tam et al.[49] as a dashed line, and the experiment of Schlinker[50] as circles. The jet operates at $M_j = 1.97$, TTR = 1.00, and $St = 0.40$ where $St$ is the Strouhal number ($fD_j u_j^{-1}$). The nozzle exit diameter is 0.0254 m. Relative to the cases used to calibrate the model, this $M_j$ is very large. Figure 3(b) shows the same predictions and measurement but at $St = 0.09$. As the frequency decreases the peak source location increases. Finally, Fig. 3(c) shows predictions and measurement for an unheated $M_j = 1.47$ jet. The equivalent source strength is integrated over the entire frequency range on a per axial location basis. Thus, Fig. 3(c), shows the total source strength at all frequencies at each axial location. The peak relative source strength is $x/D \approx 5$. Overall, the predictions of Fig. 3 generally follow the same trends as the predictions of Tam et al.[49] and the experiments of Schlinker.[50]

### Prediction of Sound Pressure Level and Coherence

Equation 38 is for the CPSD and predictions of sound pressure level (SPL) per unit St are performed by equating the observer positions. SPL is

$$\text{SPL per unit } St = 20 \log_{10} \left[ \frac{S(\boldsymbol{x}, \omega)^{1/2}}{p_{\text{ref}}} \right] + 10 \log_{10} \left[ \frac{u_j}{D_j} \right], \tag{51}$$

where $p_{\text{ref}} = 20$ $\mu$Pa is the reference pressure and $S(\boldsymbol{x}, \omega) = G(\boldsymbol{x}, \boldsymbol{x}, \omega)$ is the spectral density. The second logarithmic term is present to conserve energy when converting from PSD to SPL per unit $St$. In this paper, we compare the coherence based upon the predicted CPSD with those of corresponding measurement. The prediction of coherence is performed by evaluating

$$\Gamma(\boldsymbol{x}_1, \boldsymbol{x}_2, \omega) = \frac{G(\boldsymbol{x}_1, \boldsymbol{x}_2, \omega) G^*(\boldsymbol{x}_1, \boldsymbol{x}_2, \omega)}{G(\boldsymbol{x}_1, \boldsymbol{x}_1, \omega) G(\boldsymbol{x}_2, \boldsymbol{x}_2, \omega)}, \tag{52}$$

where superscript $*$ denotes the complex conjugate. For predictions presented within this paper, $G$ is calculated numerically using Eqn. 38.

## Survey of the Measurements

This section surveys measurements of the SHJAR facility and resultant data used for comparison with predictions. Three sets of measurements are used to validate the developed theory and consist of data from a far-field, mid-field, and near-field acoustic array. The far-field array measurements are primarily used to validate the capability to predict far-field jet noise auto-spectra over a range of jet operating conditions. The mid-field and near-field array measurements are used to validate the prediction of near-field, mid-field, and far-field outgoing wave auto-spectra and cross-spectra in the near-field and mid-field of the jet.

The design of the SHJAR facility and far-field microphone measurements were discussed by Bridges and Brown.[18] The SHJAR facility consists of a single-stream jet mounted 2.5 m above the floor within an anechoic dome with a radius of 20 m. The far-field SHJAR database of Bridges and Brown[18] has been used by many investigators. Measured auto-spectra, shown as SPL per unit $St$, were processed by Bridges and Brown. Many jet operating conditions were examined in the initial SHJAR study. Here, we select a subset of these conditions that are representative of a wide range of jet Mach numbers and temperature ratios. Conditions examined in this paper in the far-field are shown in Table 1. Each row represents a jet operating condition and each column represents the design Mach number, $M_d$, fully expanded Mach number



S. A. E. Miller, Ph.D., s.miller@nasa.gov

$M_j$, total temperature ratio, TTR, nozzle exit diameter, $D$, fully expanded velocity $u_j$, and fully expanded temperature, $T_j$. The asterisks by case names are those presented in this paper, but all were examined when developing the model. Multiple SHJAR nozzles were used and consisted of a convergent nozzle and two convergent-divergent method of characteristics $M_d = 1.185$ and $M_d = 1.50$ nozzles. The SHJAR study used a large number of microphones on a polar array of constant radius. Observer locations shown in Table 2 are used to validate the far-field SPL per unit $St$ over a range of representative jet operating conditions.

Mid-field and near-field array construction and observer placement were discussed by Suzuki and Colonius.[17] Suzuki and Colonius[17] initially designed the mid-field and near-field arrays with direct numerical simulation and experimental meanflow measurements to study jet instability waves. Figures 4 and 5 show the mid-field and near-field array respectively where 15 rings hold 78 microphones that point towards the jet centerline axis. The nozzle can be seen near the center of both arrays on the centerline axis pointing downstream. Both arrays could be moved in the axial direction to adjust the axial coordinates of the observers. Data is available for these arrays as a discrete pressure time history.

Observer positions of the mid-field array shown in Fig. 4 are plotted in Fig. 6. These observer positions are tabulated in Table 3. Figures 6(a) and 6(b) show microphone positions projected on the $x-y$ and $y-z$ planes respectively, where $x$ is the stream-wise direction, and $y$ and $z$ are orthogonal cross-stream directions. Observer positions were systematically placed to facilitate optimal statistical analysis and for potential use in beam-forming algorithms. The latter projection illustrates that the microphones were located approximately $20D$ in the radial direction from the jet centerline axis in a spiral pattern. A small circle near the origin in Fig. 6(b) represents the nozzle exit. Coordinates in both projections have been normalized by $D$.

A projection of observer positions of the near-field array of Fig. 5 are shown in Fig. 7. These observer positions are tabulated in Table 4. Figure 7(a) shows the projection in the $x-y$ plane and Fig. 7(b) shows the projection in the $y-z$ plane. Relative to the mid-field array, the microphones were arranged in a more orderly azimuthal fashion and the middle of the array was centered about the nozzle exit in the axial direction. Each subsequent axial ring was staggered azimuthally by $30^o$ which helped suppress aliasing error according to Suzuki and Colonius.[17] The spreading angle in the axial direction of the near-field array was $11.3^o$. By examining Fig. 7(b), it is observed that the radial distance of the observers from the nozzle centerline ranged from approximately $1D$ to $2.2D$. Both the near-field and mid-field arrays used quarter-inch diameter microphones.

### Data Processing

This sub-section discusses data processing of the mid-field and near-field arrays. Data processing of the far-field array was discussed by Bridges and Brown.[18] The signals from the mid-field and near-field arrays shown in Figs. 4 and 5 were converted to a discrete pressure in Pascal as a function of time. These acoustic pressures were sampled at a rate of 50 kHz and the time between sampling was $\Delta t = 2 \times 10^{-5}$ s. For each jet operating condition, the mid-field array was sampled $n_s$ =1,000,000 times and the near-field array was sampled $n_s$ = 500,000. These measurements resulted in files containing discrete pressure as a function of time for each microphone position and jet operating condition.

For both the mid-field and near-field array the PSD and SPL are required at each microphone and CPSD and coherence are required between every microphone pair. The PSD of the pressure at each microphone is

$$\mathrm{PSD}(\boldsymbol{x}, f) = \frac{2}{a_v b_w} \sum_{i=1}^{a_v} \tilde{p}(\boldsymbol{x}, t_i, \Delta t) \tilde{p}^*(\boldsymbol{x}, t_i, \Delta t) \tag{53}$$

where $a_v$ is the number of averages of the PSD, $f$ is the frequency, $p$ is the pressure, $t$ is the time at measured index value $i$, and $\boldsymbol{x}$ is the observer position measured from the nozzle exit. The variable $b_w$ is the bin-width of the resultant spectrum and is used to ensure that the PSD is on a per unit Hz basis. Recall the superscript asterisk represents the complex conjugate. A tilde represents the discrete Fourier transform from the discrete time at index $i$ to $i + n_s a_v^{-1}$. All discrete Fourier transforms are performed with the method of Ferguson.[52] For each set of array data we select $a_v = 200$. This choice results in a binwidth of 20 Hz and 10 Hz for the near- and mid-field arrays respectively. Values of $b_w$ differ between arrays because two different sample lengths are available.

The SPL per unit $St$ is calculated using Eqn. 53 as



S. A. E. Miller, Ph.D., s.miller@nasa.gov

$$\mathrm{SPL}(\boldsymbol{x}, St) = 20\log_{10}\left[\frac{\mathrm{PSD}^{1/2}}{p_{\mathrm{ref}}}\right] + 10\log_{10}\left[\frac{u_j}{D_j}\right] \tag{54}$$

where $D_j$ is the fully expanded diameter, $p_{\mathrm{ref}}$ is the reference pressure of 20 $\mu$Pa, and $u_j$ is the fully expanded jet velocity. We elect to compare prediction and measurement on a SPL per unit $St$ basis, though all predictions and measurements are performed dimensionally.

The CPSD is similarly calculated between each microphone of an array for each jet condition as

$$\mathrm{CPSD}(\boldsymbol{x}_1, \boldsymbol{x}_2, f) = \frac{2}{a_v b_w}\sum_{i=1}^{a_v}\tilde{p}(\boldsymbol{x}_1, t_i, \Delta t)\tilde{p}^*(\boldsymbol{x}_2, t_i, \Delta t). \tag{55}$$

Note that CPSD is dependent on two vector positions from the nozzle exit, $\boldsymbol{x}_1$ and $\boldsymbol{x}_2$. The CPSD is complex unlike the PSD. We prefer to compare predictions of CPSD in terms of coherence, which is a function of both PSD and CPSD. Here, we define coherence between two simultaneously captured discrete pressure time histories as

$$\Gamma(\boldsymbol{x}_1, \boldsymbol{x}_2, f) = \sum_{k=1}^{e_s}\mathrm{Re}\left[\frac{|a_v^{-1}\sum_{j=1}^{a_v}\sum_{i=1}^{e_s}\tilde{p}(\boldsymbol{x}_1, t_i, t_i+\Delta t)p^*(\boldsymbol{x}_2, t_i, t_i+\Delta t)|^2}{\left\{a_v^{-1}\sum_{j=1}^{a_v}\sum_{i=1}^{e_s}|\tilde{p}(\boldsymbol{x}_1, t_i, t_i+\Delta t)|^2\right\}\left\{a_v^{-1}\sum_{j=1}^{a_v}\sum_{i=1}^{e_s}|\tilde{p}(\boldsymbol{x}_2, t_i, t_i+\Delta t)|^2\right\}}\right] \tag{56}$$

where $e_s = n_s/a_v$ is the number of ensembles and Re is the real part (an operation to remove machine error). These statistical quantities are dependent on $f$ and are on a per unit Hz basis. Here, we prefer radial frequency, $\omega_i = 2\pi f_i$ (to be consistent with the theoretical development), and have obtained statistical quantities at discrete frequencies, $f_i = ib_w - b_w$, for $i = 2$ to $n/a_v/2$. The value of $n$ represents the number of pressures measured at time, $t$.

'Windowing' of the data during processing is not performed. Thus, some spectral leakage might be apparent in some of the measurement results. This effect is minimized because the value of $\Delta t$ is relatively small and a large number of long-averages are performed. Note that windowing is not performed in the prediction approach. Similarly, Suzuki and Colonius[17] elected not to window data for their instability wave study. Finally, the statistical quantities in Eqns. 53 through 56 are corrected to account for atmospheric absorption using the approach of Bass et al.[53,54]

## Results

This section examines predictions of the simplified model Eqn. 38 with the measured results outlined in the previous section. First, the model equation is evaluated for auto-spectra in the far-field and compared with the SHJAR polar array. Next, the model equation is evaluated for auto-spectra at the mid-field and near-field observer locations. Then the coherence between observers at the mid-field and near-field array are compared with measured coherence. Finally, a summary of a sensitivity study of the modeling parameters is presented.

### Far-Field Intensity

Figure 8 shows predicted SPL per unit $St$ for a $M_j = 1.00$ and TTR = 1.00 jet (first row of Table 1). The nozzle is convergent with an exit diameter of 0.0508 m. Observer locations are shown in Table 2 for all proceeding far-field comparisons. The observers are at various observer angles, $\Psi^o$, measured from the upstream nozzle centerline axis. Each observer is 100 nozzle diameters from the nozzle exit. Predictions and measurements are shown as solid lines with diamonds and solid lines respectively. Six auto-spectra comparisons are shown with the angle $\Psi^o$ at the left side of each comparison set. Above each set of auto-spectra the maximum SPL of the measurement is shown. Note that the vertical axis contains 20 dB per unit $St$ between major grid lines. At each observer angle the maximum SPL per unit $St$ and peak frequency is accurately captured. For small values of $\Psi^o$ the prediction slightly under-predicts the measurement due to very weak broadband shock-associated noise (BBSAN) presence near $St \approx 1.5$. The predicted spectral shape in the downstream observer direction changes relative to the sideline spectral shape automatically. In this radiation direction at relatively high or low frequencies the error is approximately 4 dB. This particular



S. A. E. Miller, Ph.D., s.miller@nasa.gov

case is important because these jet conditions are used for comparisons of the mid-field and near-field arrays. Overall, these comparisons are very satisfactory given the use of the simplified equivalent source model.

We retain the transonic Mach number and increase the heating of the jet from the previous case to TTR = 3.20. These results represent the jet operating condition shown in the third row of Table 1 and are shown in Fig. 9. The effect of refraction is smaller relative to other directions, and it is shown that the prediction and measurement compare within measurement error. This observation shows that the choice of the TTR scaling factor in the source model (Eqn. 45) is accurate and this trend is also observed in subsequent cases. The maximum SPL per unit $St$ and peak frequencies are generally captured except at $\Psi = 130^o$ where a 4 dB under-prediction of the measurement is observed. This particular angle, where the transition from incoherent mixing noise to coherent mixing noise occurs, is often difficult to predict accurately. Like the unheated transonic case, in the downstream direction the decay of predicted mixing noise intensity is too high with increasing $St$ for large $St$.

The transonic Mach number is reduced to $M_j = 0.70$ and the same TTR = 3.20 is retained relative to the previous case. This jet condition is represented by the fourth row of Table 1. Auto-spectra comparisons of this jet are shown in Fig. 10. At the sideline direction the prediction and measurement share the same maximum SPL per unit $St$ and peak frequency. The maximum SPL per unit $St$ is generally captured in the sideline and upstream direction but is under-predicted by up to 2 dB in the downstream direction. At higher frequencies in the downstream and upstream direction, the SPL per unit $St$ is under- and over-predicted by up to 8 dB respectively. At $\Psi = 150^o$ the overall spectral shape does not correctly capture the overall spectral shape of the measurement. That is, a small inflection is present near $St \approx 1$ that is not present in the prediction.

The next set of auto-spectra comparisons in the far-field are shown in Fig. 11 and represent noise intensity from an unheated $M_j = 0.40$ jet. The jet operating conditions are shown on the eighth row of Table 1. Here, the maximum noise intensity is much lower than previous cases. At the sideline location the maximum predicted SPL per unit $St$ matches measurement and peak frequency, though the lower frequencies are slightly under-predicted. Overall the maximum predicted noise intensity and peak frequency are captured and gives some credibility to the scaling factors of the source model. At very high frequencies, the same trend of over- and under-prediction is observed relative to previous cases at low and high $\Psi$ respectively.

The final far-field auto-spectra predictions are shown in Fig. 12 and the operating conditions are shown on the eleventh row of Table 1. This jet operates at $M_j = 1.185$ with moderate heating of TTR = 1.80. Overall, the maximum SPL per unit $St$ and peak intensity of the mixing noise is captured by the prediction method.

Overall, the far-field auto-spectra predictions and measurements show that the developed model for CPSD accurately captures the scaling of noise intensity with increasing jet Mach number and stagnation temperature. The model is shown to perform well over the range of available jet operating conditions. That is, it is validated for low Mach number jets through low-speed supersonic jets over a range of relevant temperature ratios. Though some of the predictions show trends of slight over- or under-prediction, overall the predictions are very good in this author's opinion given the simplicity of the equivalent source model.

### Mid-Field Intensity

We now permanently turn our attention to the transonic unheated jet ($M_j = 1.00$ and TTR = 1.00) represented by the first row of Table 1. Predictions of far-, mid-, and near-field auto-spectra using the CPSD model (Eqn. 25) are compared with measurement in Figs. 13 and 14. The observers are located at various microphone positions of the mid-field array tabulated in Table 3. Comparisons are made at locations with an asterisk by 'Mic.#' in the first column of the table. Instead of angles, $\Psi$, as in the previous far-field comparisons, these comparisons show the axial location of the microphone relative to the nozzle exit, $x_1/D$. Here, the subscript '1' denotes the location of the reference observer. For example, in Fig. 13, the second set of predictions compared with measurement from the bottom of the figure, have an $x_1/D$ location of -2.38. In Table 3, this comparison corresponds to 'Mic.#' 7, $x/D$ = -2.38, $y/D = 16.65$, $z/D = 5.41$, $\Psi^o = 82.3$, $\phi^o$ = 18.0, and $R/D = 17.66$. Note that the various observers have widely varying spatial locations, azimuthal and observer angles, and propagation distances, which supports the robustness of the model.

The maximum SPL per unit $St$ refers to the maximum measured noise intensity and a 20 $\Delta$dB range is present between major horizontal grid lines. The observer position axial location increases from the bottom to top of each figure. Once again, the measurement of the auto-spectra in SPL per unit $St$ is shown as a solid line. The prediction is represented by three lines with symbols that make up the three terms in the



S. A. E. Miller, Ph.D., s.miller@nasa.gov

developed CPSD model (Eqn. 25). A diamond, circle, and triangle represent the far-field, mid-field, and near-field contribution respectively. Note that these contributions are by name only within the integrand of the CPSD model and do not necessarily represent the dominant term in the model.

At the mid-field array the predicted noise intensity is dominated by the far-field term in the CPSD model at $St \gtrapprox 0.3$. At almost all observer angles the maximum SPL per unit $St$ and peak frequency is predicted correctly relative to measurement. In the geometric far-field, the far-field contribution propagates and is represented by the prediction shown in Fig. 8. The mid-field and near-field components of the CPSD model decay and are not represented in the corresponding far-field noise intensity predictions. At lower frequencies in the mid-field, the noise intensity is dominated by the mid-field CPSD term in the sideline and upstream direction and by the near-field CPSD term in the downstream direction. A transition occurs from mid-field to near-field dominance of the noise intensity near $x_1/D = 19.38$. At axial observer locations smaller than $x_1/D = 15.63$, the magnitude and peak of the prediction is correctly captured by the mid-field term relative to measurement at low frequencies. After the transition at axial location $x_1/D = 19.38$, the near-field term of the CPSD model starts to dominate and captures the rising low-frequency peak observed in the measurements near $St \approx 0.004$. Overall, the predicted SPL per unit $St$ at the mid-field array compares very favorably with measurement.

### Near-Field Intensity

The final auto-spectra predictions, for the unheated transonic jet, are shown in Fig. 15 at the near-field array locations tabulated by Table 4. Asterisks in the table represent observer locations where comparisons are conducted. Note that the observer positions represent a wide range of axial locations and widely varying propagation distances. The format of Fig. 15 is the same as Figs. 13 and 14. In the upstream and partly in the sideline direction strong partially broad tones are observed in the measurement. These tones were shown to correspond to acoustic-modes in a quiescent flow from a cylindrical pipe by Suzuki and Colonius[17] and are not due to jet mixing noise. Their effect, in the upstream direction and their eventually broadening and decay in the downstream direction, dominates the measurement at all large $St$. Thus, they should be disregarded when assessing the comparisons. Furthermore, at high $St$ the incident angle of the microphones relative to incoming sound waves at high frequencies causes an artificial broadening of intensity in the data.

The far-field contribution is shown as the line with diamonds. At $x_1/D = -0.875$ the interior nozzle tones dominate the prediction and make assessing its validity difficult. However, as the axial observer position is increased a clear broad contribution of the far-field CPSD term is apparent with measurement. For example, at $x_1/D = 5.375$, the prediction is 2 dB lower than the measured peak intensity. The mid-field contribution of the CPSD model matches in magnitude with the measurement for $St \approx 0.05$, especially at the downstream axial observer locations. The low-frequencies are generally dominated by the near-field term, but unfortunately measurement is not available at such low frequencies in the upstream and sideline direction. In the downstream radiation direction, the near-field spectral peak frequency is too high and too intense relative to measurement by 10 dB. Overall, given the difficulty of accurately predicting near-field jet noise, the predictions are relatively good compared to the measurement. We are able to predict with a single equation and with confidence, the near-field, mid-field, and far-field noise intensity, using a CPSD acoustic analogy.

### Mid-Field Coherence

We now turn our attention to the prediction of coherence between observers in the mid-field. Coherence is predicted using Eqn. 52 and compared to the measured coherence calculated using Eqn. 56. The jet operates at the unheated transonic condition represented by the first row of Table 1. Figure 16 shows coherence as a function of $St$ for various observer pairs separated by azimuthal angle, $\phi$, at four axial locations. These plots of azimuthally varying coherence are representative of the other axial locations. The axial locations are $x/D = 0$, $x/D = 5.25$, $x/D = 15.63$, and $x/D = 28.63$ shown in Fig. 16(a) through 16(d) respectively. The respective figure legends show $\Delta\phi^o$ between observer pairs at each axial location. The reference observer locations can be ascertained easily from Table 3.

Figure 16(a) represents the azimuthal coherence variation in the sideline direction of the mid-field array. The lines and associated line types with symbols are pairs of measured and predicted coherence respectively. For an observer separation of $\Delta\phi = 60^o$ the agreement between the prediction and measurement is very good. As the angle $\phi$ is increased between the observer pairs the coherence decreases. Generally, higher



S. A. E. Miller, Ph.D., s.miller@nasa.gov

coherence is predicted at lower $St$ and is nearly zero at higher $St$. The prediction in Fig. 16(d) at low $St$ and high $St$ is in agreement with measurement, however there resides a small broad peak near $St \approx 0.2$ that is not predicted. These predictions and measurements involving azimuthal decay agree with the trends predicted by Ribner.[15]

Figure 17 shows variation of coherence from the transonic unheated jet in the mid-field with varying axial and azimuthal observer pairs. The reference observer number in Figs. 17(a) and 17(b) is 1 and 43 respectively. These represent the coherence decay relative to the upstream observer and an observer in the middle of the array. Observers used in this axial coherence comparison are shown in Table 3 with diamond superscripts. In Fig. 17(a), the reference observer is at $x_1/D = -5.13$ and the paired observers are at $\Delta x_1/D = 2.75$, 8.76, 12.38, and 28.76 respectively. The varying axial separations of Fig. 17(b) are $\Delta x_1/D =$ -12.01, -6.00, 9.75, and 19.00. Note there is an associated $\Delta\phi$ for each observer set with similar delta off-sets. At low and high frequencies, $St \approx 0.01$ and $St \approx 10$, the magnitude of the coherence has been captured with both varying axial distance and azimuthal angle. In some cases the coherence is predicted very satisfactory, such as in Fig. 17(a) for observer 1 and 65 or Fig. 17(b) for observer 43 and 25. In these cases the shape of the coherence and its magnitude match measurement throughout the range of $St$. Unfortunately, for some observer pairs in Fig. 17 the shape of coherence with $St$ is less satisfactory. For example, in Fig. 17(a) observer pair 1 and 7, the predictions show a much greater coherent decay with increasing $St$. In both the prediction and measurement, we observe that the coherence transforms from a Gaussian shape to an exponentially decreasing shape with increasing axial and azimuthal separation, which is also in agreement with the measurements of Viswanathan.[20]

### Near-Field Coherence

Coherence between observer pairs of the near-field array are now examined. Coherence with varying $\Delta\phi$ at constant axial locations is shown in Fig. 18 and follows the same format as Fig. 16. The axial reference positions are at $x_1/D =$ -0.88, 0.38, 2.25, and 4.75 and are shown in Figs. 18(a) through 18(d) respectively. The observer pairs are incremented by $\Delta\phi = 60^o$. Relative to the mid-field array azimuthal coherence measurements shown in Fig. 16, extremely strong coherence peaks are observed in the range $0.01 \lessapprox St \lessapprox 1.1$. As the axial position of the reference observer increases, these peaks of coherence decrease and broaden into a large single contribution near $St \approx 0.4$, as shown in Fig. 18(d). These are due to the tones previously discussed in the near-field SPL per unit $St$ comparisons of Fig. 15. Within the ranges $0.01 \lessapprox St \lessapprox 0.1$ and $St \gtrapprox 1$, the agreement between prediction and measurement is satisfactory and captures the overall trends of the azimuthally varying coherence at constant axial positions. Otherwise, it is difficult to assess the prediction due to the near-field tones.

The final set of near-field predictions is shown in Fig. 19 for axially and azimuthally varying coherence. The jet operates at the transonic and unheated condition. The reference observers are 13 and 37 shown in Table 4 and diamond superscripts denote observer pairs. Reference observers 13 and 37 are at the upstream and middle locations of the near-field array. Axial separations in Fig. 19(a) are $\Delta x_1/D =$ 1.26, 3.12, 4.38, 5.63 and are $\Delta x_1/D =$ -1.88, -0.63, 1.25 and 2.50 respectively. Like the azimuthally varying coherence comparisons shown previously, strong broad coherent peaks are present within the coherence of the near-field. Predictions do not illustrate the complete transition from a Gaussian coherence with increasing $St$ to an exponential decay with increasing $St$. However, we can observe the beginning of the transition. This partial transition is observed in Fig. 19(a) between observers 13 and 25 and in Fig. 19(b) between observers 37 and 19. Discounting the multiple coherent peaks, the variation of coherence with $St$ is overall satisfactory given the difficulty of the calculation and measurement. The predicted coherence between observer positions 37 and 61 shows a rise in coherence near $St \approx 2$. This is likely due to the formation of the cross-spectral acoustic analogy and unlikely due to the formulation of the source model. The decay of the near-field coherence with increasing axial location generally shows the correct decay at $St \approx 0.03$ through $St \approx 3$.

Overall, the near-field array predicted coherence shows more variation from measurement than the mid-field coherence. This is partly due to the contamination of the measurement by laboratory scale interior nozzle tones. The near-field coherence predictions, unlike the mid-field, contain strong dominance from the near-field equivalent source term. The combination of accurate near-field jet noise intensity predictions shown in Fig. 15 and coherence predictions shown in Figs. 18 and 19 allow for the acoustic loading in the jet near-field to be quantified. The combination of near-field noise intensity and coherence allow for the quantitative coupling between jet fluid dynamics, jet aeroacoustics, and airframe structure, using an approach that is more analytical than any other.



S. A. E. Miller, Ph.D., s.miller@nasa.gov

### Sensitivity Analysis

A sensitivity analysis is performed on the parameters that are present within the source model equations. The numerical one-at-a-time sensitivity approach is selected. It is feasible to perform an analytical one-at-a-time sensitivity approach by performing partial derivatives of the model equation relative to each term, though, this approach is prohibitively time intensive. We vary the magnitude of each parameter by one percent and observe the magnitude of the change in the spectral density. The base case selected is the transonic unheated jet that is used for the majority of the validation. Two near-field observers are selected so that the sensitivity of the near- and mid-field terms are included in the analysis. These observers are located at microphones 19 and 43 of the near-field array as shown in Table 4. Figures 20(a) and 20(b) show the one-at-a-time sensitivity study for the most sensitive model parameters for the chosen base case as a function of $St$. Note the $y$-axis is the absolute change in SPL per unit $St$ relative to the base case intensity. The dominant sensitive parameters in Fig. 20(a) are $k_{\max}$, $\overline{u}$, and at very high frequencies $l_s$. At the downstream observer location $M_c$ is most sensitive. Note that some parameters are frequency independent or angle dependent. No single modeling parameter altered the model response by more than a dB in the numerical one-at-a-time sensitivity study. These results are characteristic for the other jet Mach numbers, temperatures, and near-field observer positions examined.

## Conclusion

An acoustic analogy is developed that predicts the CPSD from turbulent flow. It includes near-field, mid-field, and far-field terms and the effect of an ambient Mach number. Unfortunately, measurement data are not available to validate cross-spectral predictions with a non-zero ambient Mach number. One simple equivalent source model, that is a function of the jet operating conditions and the two-point cross-correlation of the Lighthill stress tensor, is proposed and yields accurate prediction of near-field CPSD. The CPSD model transitions to a traditional auto-spectral model in the far-field automatically. Spectra and coherence compare favorably with measurement in the near-field, mid-field, and far-field for a wide range of jet Mach numbers and temperature ratios.

Given the difficulty of predicting near-field jet noise intensity, let alone CPSD and associated coherence, the use of a simple equivalent source captures the overall trends and in many cases produces excellent predictions relative to measurement. The knowledge of the noise intensity and its spatial coherent decay on a per frequency basis allows for the loading on flight vehicle airframes to be quantified. These predictions allow for estimation of interior vibration, noise, and fatigue estimates with appropriate coupled structural models.

An equivalent source model is selected for its speed, and a more physical model based on steady RANS solutions is proposed in the appendix. This latter modeling approach can directly relate meanflow solutions from more realistic engine nozzles to the CPSD but carries a very high computational cost. The source model proposed in the paper can easily be improved to include other effects, such as a secondary stream or use measurements from acoustic arrays involving source strength per unit length.

## Acknowledgements

This paper is dedicated to Herbert S. Ribner of the University of Toronto Institute for Aerospace Studies. The author benefited from discussions and an introduction to this problem by his colleague Daniel L. Palumbo of the National Aeronautics and Space Administration (NASA) Langley Research Center. The author is thankful for continuous support from the NASA Fundamental Aeronautics Program High Speed Project.

## Appendix: A Steady Reynolds-Averaged Navier-Stokes Source Model

This section surveys the development and implementation of the CPSD model with the use of a steady RANS solution. By using this alternative approach the CPSD can be directly linked to industrial jet flow solutions. This dependence relies on accurate modeling of the flows with modern CFD. We return to Eqn. 35 which is repeated here for convenience,

$$G\left(\boldsymbol{x}_1, \boldsymbol{x}_2, \omega\right) = \frac{1}{16\pi^2} \int_{-\infty}^{\infty} ... \int_{-\infty}^{\infty} \frac{A_{ijlm} l_s}{\overline{u}} \left\{F_t \omega^4 + M_t \omega^2 + N_t\right\}$$
$$\times \exp\left[\frac{-i\xi\omega}{\overline{u}}\right] \exp\left[\frac{-|\xi|}{\overline{u}\tau_s}\right] \exp\left[\frac{-\eta^2}{l_{sy}^2}\right] \exp\left[\frac{-\zeta^2}{l_{sz}^2}\right] \exp\left[\frac{-l_s^2\omega^2}{4\overline{u}^2}\right] \exp\left[\frac{-i\omega(r-r')}{c_\infty}\right] d\boldsymbol{\eta}' d\boldsymbol{\eta}, \tag{57}$$

where $F_t$, $M_t$, and $N_t$ are given by Eqns. 20 through 22 respectively. The streamwise mean velocity component, $\overline{u}$, is directly dependent on the steady RANS solution. The turbulent length and time scales, $l_s$ and $\tau_s$, are functions of the steady RANS solution. We estimate them using,

$$l_s = l_c k^{3/2}/\epsilon, \tag{58}$$

and,

$$\tau_s = \tau_c k/\epsilon, \tag{59}$$

where $l_c = 1.00$ and $\tau_c = 0.05$ are constant coefficients. These coefficients have been calibrated based on a steady RANS solution produced by the NASA Langley Fully-Unstructured Navier-Stokes (FUN3D) CFD code and acoustic intensities for the cold transonic jet. Cross-stream turbulent length scales, $l_{sy}$ and $l_{sz}$, are one-third of $l_s$. The model for $A_{ijlm}$ is altered,

$$A_{ijlm} = P_{f2} A_{ij} A_{lm}, \tag{60}$$

where $P_{f2} = \pi(10^{3/10})^2$. The definition of $A_{ij}$ and $A_{lm}$ is given by Eqn. 40. The subsequent dependent variables of $A_{ij}$ and $A_{lm}$ are dependent on the local Mach number instead of $M_j$. Equations 45 through 50 are not applicable for a steady RANS based model. Strategies for obtaining the steady RANS solution, its validation, implementation of this model, and its integration with the steady RANS solution is beyond the scope of this appendix. The evaluation of Eqn. 57 is computationally expensive due to the many summations within the integrand and due to the double volumetric spatial integrals involving $\boldsymbol{\eta}'$ and $\boldsymbol{\eta}$. Nonetheless, for the transonic case examined, the predictions have the same relative agreement with measurement as previously shown.



S. A. E. Miller, Ph.D., s.miller@nasa.gov

# Tables

**Table 1. Jet operating conditions. Asterisks denote cases shown in this paper.**

| Case Name | $M_d$ | $M_j$ | TTR | $D$ (m) | $u_j$ (m/s) | $T_j$ (K) |
|---|---|---|---|---|---|---|
| SMC0001* | 1.00 | 1.00 | 1.00 | 0.0508 | 313.2 | 244.2 |
| SMC0004 | 1.00 | 1.00 | 2.70 | 0.0508 | 514.7 | 659.3 |
| SMC0007* | 1.00 | 1.00 | 3.20 | 0.0508 | 560.3 | 781.3 |
| SMC00010* | 1.00 | 0.70 | 3.20 | 0.0508 | 410.0 | 853.9 |
| SMC00012 | 1.00 | 0.70 | 1.00 | 0.0508 | 229.2 | 266.8 |
| SMC00014 | 1.00 | 0.50 | 1.00 | 0.0508 | 167.4 | 279.0 |
| SMC00016 | 1.00 | 0.50 | 2.20 | 0.0508 | 248.3 | 613.9 |
| SMC00018* | 1.00 | 0.40 | 1.00 | 0.0508 | 135.1 | 283.9 |
| SMC00019 | 1.00 | 0.40 | 2.70 | 0.0508 | 222.0 | 766.6 |
| SMC0141 | 1.185 | 1.185 | 1.00 | 0.0508 | 359.3 | 228.8 |
| SMC0142* | 1.185 | 1.185 | 1.80 | 0.0508 | 482.0 | 411.8 |
| SMC0143 | 1.185 | 1.185 | 3.00 | 0.0508 | 622.3 | 686.3 |
| SMC0164 | 1.50 | 1.500 | 1.00 | 0.0508 | 427.4 | 202.1 |

**Table 2. Far-field microphone array.**

| Microphone | $x/D$ | $y/D$ | $z/D$ | $\Psi^o$ | $\phi^o$ | $R/D$ |
|---|---|---|---|---|---|---|
| 1 | 86.60 | 50.00 | 0 | 150.0 | 0 | 100 |
| 2 | 64.28 | 76.60 | 0 | 130.0 | 0 | 100 |
| 3 | 34.20 | 93.97 | 0 | 110.0 | 0 | 100 |
| 4 | 0 | 100.00 | 0 | 90.0 | 0 | 100 |
| 5 | -34.20 | 93.97 | 0 | 70.0 | 0 | 100 |
| 6 | -64.28 | 76.60 | 0 | 50.0 | 0 | 100 |



S. A. E. Miller, Ph.D., s.miller@nasa.gov

**Table 3. Mid-field microphone locations. Asterisks denote microphones for SPL validation and the reference microphone for circumferential coherence validation. Diamonds denote microphones used for axial coherence validation.**

| Mic.# | $x/D$ | $y/D$ | $z/D$ | $\Psi^o$ | $\phi^o$ | $R/D$ | Mic.# | $x/D$ | $y/D$ | $z/D$ | $\Psi^o$ | $\phi^o$ | $R/D$ |
|---|---|---|---|---|---|---|---|---|---|---|---|---|---|
| 1*◇ | -5.13 | 17.50 | 0 | 73.7 | 0 | 18.24 | 40 | 7.25 | -12.63 | -14.03 | 111.0 | -132.0 | 20.22 |
| 2 | -5.13 | 8.75 | 15.16 | 73.7 | 60.0 | 18.23 | 41 | 7.25 | 5.83 | -17.95 | 111.0 | -72.0 | 20.22 |
| 3 | -5.13 | -8.75 | 15.16 | 73.7 | 120.0 | 18.23 | 42◇ | 7.25 | 18.46 | -3.93 | 111.0 | -12.0 | 20.22 |
| 4 | -5.13 | -17.50 | 0 | 73.7 | 180.0 | 18.24 | 43* | 9.63 | 19.14 | 2.01 | 116.6 | 6.0 | 21.52 |
| 5 | -5.13 | -8.75 | -15.16 | 73.7 | -120.0 | 18.23 | 44 | 9.63 | 7.83 | 17.59 | 116.6 | 66.0 | 21.52 |
| 6 | -5.13 | 8.75 | -15.16 | 73.7 | -60.0 | 18.23 | 45 | 9.63 | -11.32 | 15.57 | 116.6 | 126.0 | 21.52 |
| 7*◇ | -2.38 | 16.65 | 5.41 | 82.3 | 18.0 | 17.66 | 46 | 9.63 | -19.14 | -2.01 | 116.6 | -174.0 | 21.52 |
| 8 | -2.38 | 3.64 | 17.12 | 82.3 | 78.0 | 17.66 | 47 | 9.63 | -7.83 | -17.59 | 116.6 | -114.0 | 21.52 |
| 9 | -2.38 | -13.01 | 11.71 | 82.3 | 138.0 | 17.66 | 48 | 9.63 | 11.32 | -15.57 | 116.6 | -54.0 | 21.52 |
| 10 | -2.38 | -16.64 | -5.41 | 82.3 | -162.0 | 17.66 | 49*◇ | 12.38 | 18.04 | 8.03 | 122.1 | 24.0 | 23.31 |
| 11 | -2.38 | -3.64 | -17.12 | 82.3 | -102.0 | 17.66 | 50 | 12.38 | 2.06 | 19.64 | 122.1 | 84.0 | 23.31 |
| 12 | -2.38 | 13.01 | -11.71 | 82.3 | -42.0 | 17.66 | 51 | 12.38 | -15.98 | 11.61 | 122.1 | 144.0 | 23.31 |
| 13* | 0 | 14.16 | 10.29 | 90.0 | 36.0 | 17.50 | 52 | 12.38 | -18.04 | -8.03 | 122.1 | -156.0 | 23.31 |
| 14 | 0 | -1.83 | 17.40 | 90.0 | 96.0 | 17.50 | 53 | 12.38 | -2.06 | -19.64 | 122.1 | -96.0 | 23.31 |
| 15 | 0 | -15.99 | 7.12 | 90.0 | 156.0 | 17.50 | 54 | 12.38 | 15.98 | -11.61 | 122.1 | -36.0 | 23.31 |
| 16 | 0 | -14.16 | -10.29 | 90.0 | -144.0 | 17.50 | 55* | 15.63 | 15.16 | 13.63 | 127.5 | 42.0 | 25.69 |
| 17◇ | 0 | 1.83 | -17.40 | 90.0 | -84.0 | 17.50 | 56 | 15.63 | -4.24 | 19.93 | 127.5 | 102.0 | 25.68 |
| 18 | 0 | 15.99 | -7.12 | 90.0 | -24.0 | 17.50 | 57 | 15.63 | -19.38 | 6.30 | 127.5 | 162.0 | 25.68 |
| 19* | 2.00 | 10.51 | 14.46 | 96.4 | 54.0 | 17.99 | 58 | 15.63 | -15.17 | -13.63 | 127.5 | -138.0 | 25.69 |
| 20 | 2.00 | -7.27 | 16.33 | 96.4 | 114.0 | 17.99 | 59 | 15.63 | 4.24 | -19.93 | 127.5 | -78.0 | 25.68 |
| 21 | 2.00 | -17.78 | 1.87 | 96.4 | 174.0 | 17.99 | 60◇ | 15.63 | 19.38 | -6.30 | 127.5 | -18.0 | 25.68 |
| 22 | 2.00 | -10.51 | -14.46 | 96.4 | -126.0 | 17.99 | 61* | 19.38 | 9.53 | 18.71 | 132.7 | 63.0 | 28.57 |
| 23 | 2.00 | 7.27 | -16.33 | 96.4 | -66.0 | 17.99 | 62 | 19.38 | -18.71 | 9.53 | 132.7 | 153.0 | 28.57 |
| 24◇ | 2.00 | 17.78 | -1.87 | 96.4 | -6.0 | 17.99 | 63 | 19.38 | -9.53 | -18.71 | 132.7 | -117.0 | 28.57 |
| 25*◇ | 3.63 | 17.73 | 3.77 | 101.3 | 12.0 | 18.48 | 64◇ | 19.38 | 18.71 | -9.53 | 132.7 | -27.0 | 28.57 |
| 26 | 3.63 | 5.60 | 17.24 | 101.3 | 72.0 | 18.48 | 65*◇ | 23.63 | 19.49 | 9.93 | 137.2 | 27.0 | 32.20 |
| 27 | 3.63 | -12.13 | 13.47 | 101.3 | 132.0 | 18.48 | 66 | 23.63 | -9.93 | 19.49 | 137.2 | 117.0 | 32.20 |
| 28 | 3.63 | -17.73 | -3.77 | 101.3 | -168.0 | 18.48 | 67 | 23.63 | -19.49 | -9.93 | 137.2 | -153.0 | 32.20 |
| 29 | 3.63 | -5.60 | -17.24 | 101.3 | -108.0 | 18.48 | 68 | 23.63 | 9.93 | -19.49 | 137.2 | -63.0 | 32.20 |
| 30 | 3.63 | 12.13 | -13.47 | 101.3 | -48.0 | 18.49 | 69* | 28.63 | 3.56 | 22.47 | 141.5 | 81.0 | 36.56 |
| 31*◇ | 5.25 | 16.03 | 9.25 | 105.8 | 30.0 | 19.23 | 70 | 28.63 | -22.47 | 3.56 | 141.5 | 171.0 | 36.56 |
| 32 | 5.25 | 0 | 18.50 | 105.8 | 90.0 | 19.23 | 71 | 28.63 | -3.56 | -22.47 | 141.5 | -99.0 | 36.56 |
| 33 | 5.25 | -16.03 | 9.25 | 105.8 | 150.0 | 19.23 | 72◇ | 28.63 | 22.47 | -3.56 | 141.5 | -9.0 | 36.56 |
| 34 | 5.25 | -16.03 | -9.25 | 105.8 | -150.0 | 19.23 | 73* | 34.38 | 16.79 | 16.79 | 145.4 | 45.0 | 41.78 |
| 35 | 5.25 | 0 | -18.50 | 105.8 | -90.0 | 19.23 | 74 | 34.38 | -16.79 | 16.79 | 145.4 | 135.0 | 41.78 |
| 36 | 5.25 | 16.03 | -9.25 | 105.8 | -30.0 | 19.23 | 75 | 34.38 | -16.79 | -16.79 | 145.4 | -135.0 | 41.78 |
| 37* | 7.25 | 12.63 | 14.03 | 111.0 | 48.0 | 20.22 | 76 | 34.38 | 16.79 | -16.79 | 145.4 | -45.0 | 41.78 |
| 38 | 7.25 | -5.83 | 17.95 | 111.0 | 108.0 | 20.22 | 77◇ | 41.00 | 24.69 | 3.91 | 148.6 | 9.0 | 48.02 |
| 39 | 7.25 | -18.46 | 3.92 | 111.0 | 168.0 | 20.22 | 78 | 41.00 | -3.91 | 24.69 | 148.6 | 99.0 | 48.02 |



S. A. E. Miller, Ph.D., s.miller@nasa.gov

**Table 4. Near-field microphone locations. Asterisks denote microphones for SPL validation and the reference microphone for circumferential coherence validation. Diamonds denote microphones used for axial coherence validation.**

| Mic.# | $x/D$ | $y/D$ | $z/D$ | $\Psi^o$ | $\phi^o$ | $R/D$ | Mic.# | $x/D$ | $y/D$ | $z/D$ | $\Psi^o$ | $\phi^o$ | $R/D$ |
|---|---|---|---|---|---|---|---|---|---|---|---|---|---|
| 1 | -2.13 | 0.76 | 0.44 | 22.4 | 30.0 | 2.30 | 40 | 1.63 | -1.41 | -0.81 | 135.0 | 210.0 | 2.30 |
| 2 | -2.13 | 0 | 0.88 | 22.4 | 90.0 | 2.30 | 41 | 1.63 | 0 | -1.63 | 135.0 | 270.0 | 2.30 |
| 3 | -2.13 | -0.76 | 0.44 | 22.4 | 150.0 | 2.30 | 42 | 1.63 | 1.41 | -0.81 | 135.0 | 330.0 | 2.30 |
| 4 | -2.13 | -0.76 | -0.44 | 22.4 | 210.0 | 2.30 | 43*◇ | 2.25 | 1.75 | 0 | 142.1 | 0 | 2.85 |
| 5 | -2.13 | 0 | -0.88 | 22.4 | 270.0 | 2.30 | 44 | 2.25 | 0.88 | 1.52 | 142.1 | 60.0 | 2.85 |
| 6 | -2.13 | 0.76 | -0.44 | 22.4 | 330.0 | 2.30 | 45 | 2.25 | -0.88 | 1.52 | 142.1 | 120.0 | 2.85 |
| 7 | -1.50 | 1.00 | 0 | 33.7 | 0 | 1.80 | 46 | 2.25 | -1.75 | 0 | 142.1 | 180.0 | 2.85 |
| 8 | -1.50 | 0.50 | 0.87 | 33.7 | 60.0 | 1.80 | 47 | 2.25 | -0.88 | -1.52 | 142.1 | 240.0 | 2.85 |
| 9 | -1.50 | -0.50 | 0.87 | 33.7 | 120.0 | 1.80 | 48 | 2.25 | 0.88 | -1.52 | 142.1 | 300.0 | 2.85 |
| 10 | -1.50 | -1.00 | 0 | 33.7 | 180.0 | 1.80 | 49*◇ | 2.88 | 1.62 | 0.94 | 146.9 | 30.0 | 3.43 |
| 11 | -1.50 | -0.50 | -0.87 | 33.7 | 240.0 | 1.80 | 50 | 2.88 | 0 | 1.88 | 146.9 | 90.0 | 3.43 |
| 12 | -1.50 | 0.50 | -0.87 | 33.7 | 300.0 | 1.80 | 51 | 2.88 | -1.62 | 0.94 | 146.9 | 150.0 | 3.43 |
| 13*◇ | -0.88 | 0.97 | 0.56 | 52.1 | 30.0 | 1.43 | 52 | 2.88 | -1.62 | -0.94 | 146.9 | 210.0 | 3.43 |
| 14 | -0.88 | 0 | 1.13 | 52.1 | 90.0 | 1.43 | 53 | 2.88 | 0 | -1.88 | 146.9 | 270.0 | 3.43 |
| 15 | -0.88 | -0.97 | 0.56 | 52.1 | 150.0 | 1.43 | 54 | 2.88 | 1.62 | -0.94 | 146.9 | 330.0 | 3.43 |
| 16 | -0.88 | -0.97 | -0.56 | 52.1 | 210.0 | 1.43 | 55*◇ | 3.50 | 2.00 | 0 | 150.3 | 0 | 4.03 |
| 17 | -0.88 | 0 | -1.13 | 52.1 | 270.0 | 1.43 | 56 | 3.50 | 1.00 | 1.73 | 150.3 | 60.0 | 4.03 |
| 18 | -0.88 | 0.97 | -0.56 | 52.1 | 330.0 | 1.43 | 57 | 3.50 | -1.00 | 1.73 | 150.3 | 120.0 | 4.03 |
| 19*◇ | -0.25 | 1.25 | 0 | 78.7 | 0 | 1.27 | 58 | 3.50 | -2.00 | 0 | 150.3 | 180.0 | 4.03 |
| 20 | -0.25 | 0.63 | 1.08 | 78.7 | 60.0 | 1.27 | 59 | 3.50 | -1.00 | -1.73 | 150.3 | 240.0 | 4.03 |
| 21 | -0.25 | -0.63 | 1.08 | 78.7 | 120.0 | 1.27 | 60 | 3.50 | 1.00 | -1.73 | 150.3 | 300.0 | 4.03 |
| 22 | -0.25 | -1.25 | 0 | 78.7 | 180.0 | 1.27 | 61*◇ | 4.13 | 1.84 | 1.06 | 152.7 | 30.0 | 4.64 |
| 23 | -0.25 | -0.63 | -1.08 | 78.7 | 240.0 | 1.27 | 62 | 4.13 | 0 | 2.13 | 152.7 | 90.0 | 4.64 |
| 24 | -0.25 | 0.63 | -1.08 | 78.7 | 300.0 | 1.27 | 63 | 4.13 | -1.84 | 1.06 | 152.7 | 150.0 | 4.64 |
| 25*◇ | 0.38 | 1.19 | 0.69 | 105.3 | 30.0 | 1.43 | 64 | 4.13 | -1.84 | -1.06 | 152.7 | 210.0 | 4.64 |
| 26 | 0.38 | 0 | 1.38 | 105.3 | 90.0 | 1.43 | 65 | 4.13 | 0 | -2.13 | 152.7 | 270.0 | 4.64 |
| 27 | 0.38 | -1.19 | 0.69 | 105.3 | 150.0 | 1.43 | 66 | 4.13 | 1.84 | -1.06 | 152.7 | 330.0 | 4.64 |
| 28 | 0.38 | -1.19 | -0.69 | 105.3 | 210.0 | 1.43 | 67*◇ | 4.75 | 2.25 | 0 | 154.7 | 0 | 5.26 |
| 29 | 0.38 | 0 | -1.38 | 105.3 | 270.0 | 1.43 | 69 | 4.75 | -1.13 | 1.95 | 154.7 | 120.0 | 5.26 |
| 30 | 0.38 | 1.19 | -0.69 | 105.3 | 330.0 | 1.43 | 70 | 4.75 | -2.25 | 0 | 154.7 | 180.0 | 5.26 |
| 31*◇ | 1.00 | 1.50 | 0 | 123.7 | 0 | 1.80 | 71 | 4.75 | -1.13 | -1.95 | 154.7 | 240.0 | 5.26 |
| 32 | 1.00 | 0.75 | 1.30 | 123.7 | 60.0 | 1.80 | 72 | 4.75 | 1.13 | -1.95 | 154.7 | 300.0 | 5.26 |
| 33 | 1.00 | -0.75 | 1.30 | 123.7 | 120.0 | 1.80 | 73*◇ | 4.75 | 2.06 | 1.19 | 154.7 | 30.0 | 5.88 |
| 34 | 1.00 | -1.50 | 0 | 123.7 | 180.0 | 1.80 | 74 | 5.38 | 0 | 2.38 | 156.2 | 90.0 | 5.88 |
| 35 | 1.00 | -0.75 | -1.30 | 123.7 | 240.0 | 1.80 | 75 | 5.38 | -2.06 | 1.19 | 156.2 | 150.0 | 5.88 |
| 36 | 1.00 | 0.75 | -1.30 | 123.7 | 300.0 | 1.80 | 68 | 5.38 | 1.13 | 1.95 | 156.2 | 60.0 | 5.26 |
| 37 | 1.63 | 1.41 | 0.81 | 135.0 | 30.0 | 2.30 | 76 | 5.38 | -2.06 | -1.19 | 156.2 | 210.0 | 5.88 |
| 38 | 1.63 | 0 | 1.63 | 135.0 | 90.0 | 2.30 | 77 | 5.38 | 0 | -2.38 | 156.2 | 270.0 | 5.88 |
| 39 | 1.63 | -1.41 | 0.81 | 135.0 | 150.0 | 2.30 | 78*◇ | 5.38 | 2.06 | -1.19 | 156.2 | 330.0 | 5.88 |



S. A. E. Miller, Ph.D., s.miller@nasa.gov

# Figures

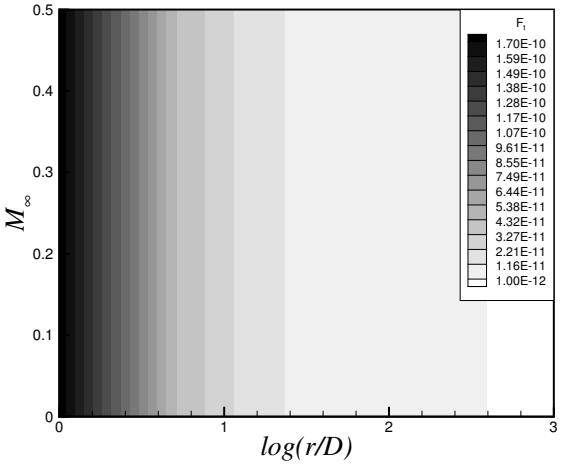


(a) The far-field term.

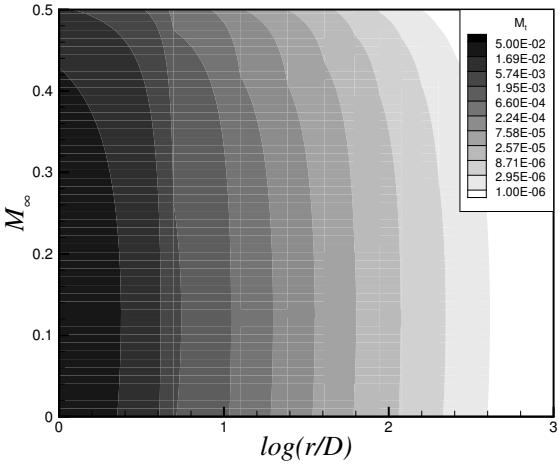


(b) The mid-field term.

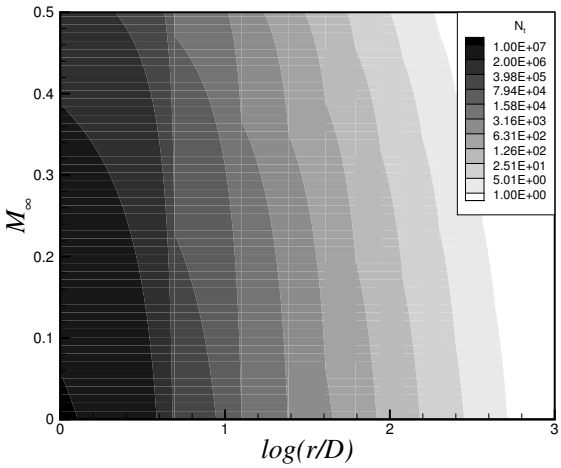


(c) The near-field term.

**Figure 1. Variation of $F_t$, $M_t$, and $N_t$ with flight stream Mach number and sideline observer position.**



S. A. E. Miller, Ph.D., s.miller@nasa.gov

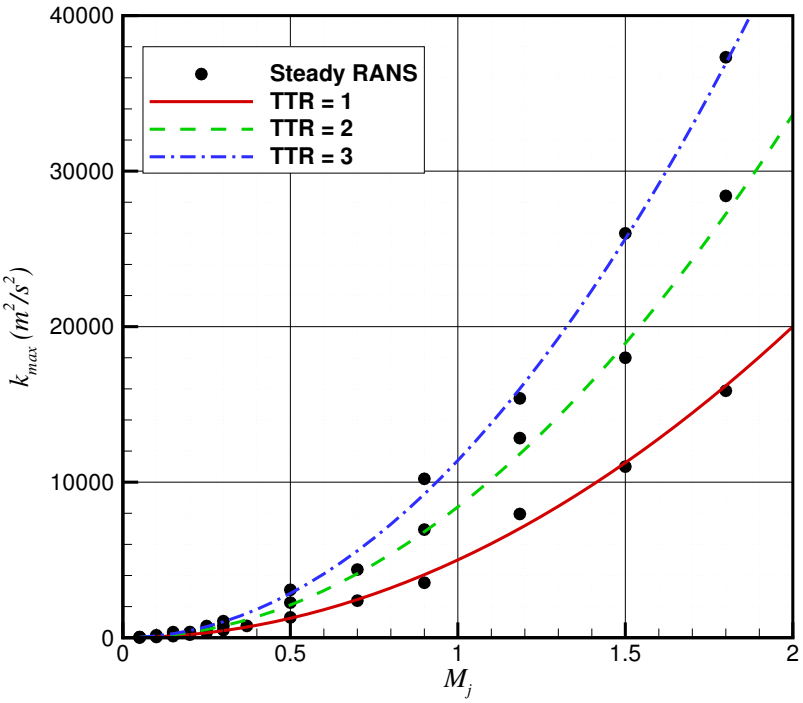


**Figure 2. Comparison of the model for maximum $k$ within the jet plume compared to various steady RANS predictions.**



S. A. E. Miller, Ph.D., s.miller@nasa.gov

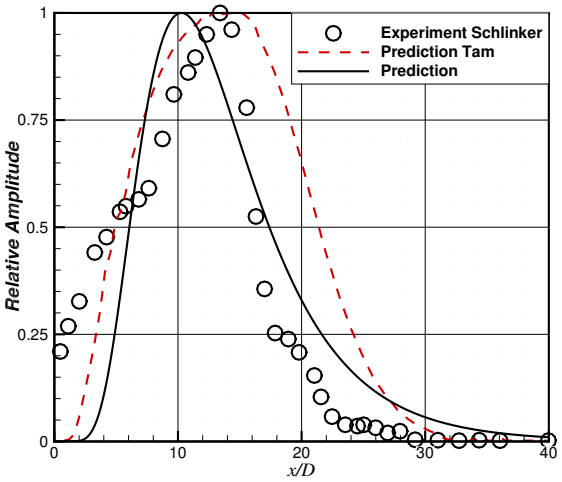


(a) A $M_j = 1.97$ unheated jet at $St = 0.40$.

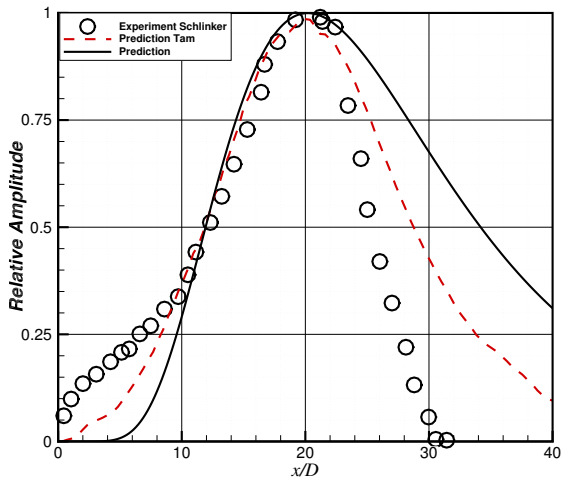


(b) A $M_j = 1.97$ unheated jet at $St = 0.09$.

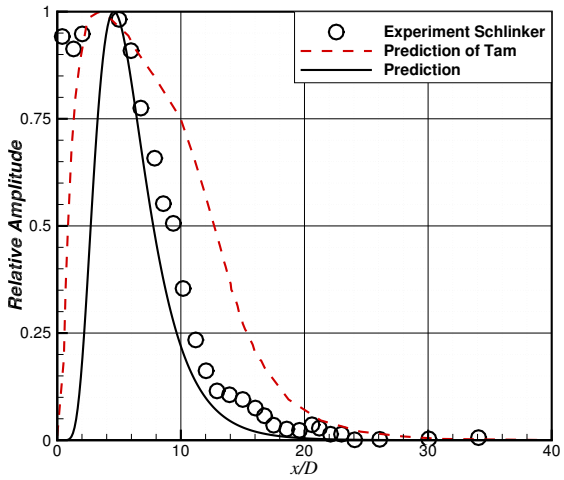


(c) A $M_j = 1.47$ unheated jet and the source is cumulative.

**Figure 3. Predictions of relative source strength per unit length compared to predictions of Tam and measurements of Schlinker.**

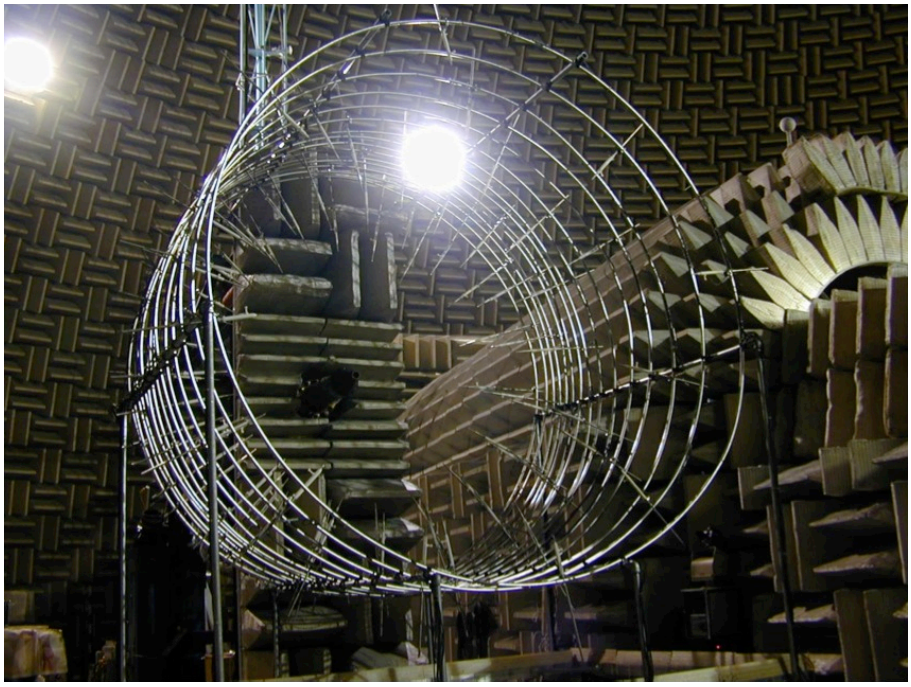

**Figure 4. The mid-field array.**

**Figure 5. The near-field array.**



S. A. E. Miller, Ph.D., s.miller@nasa.gov

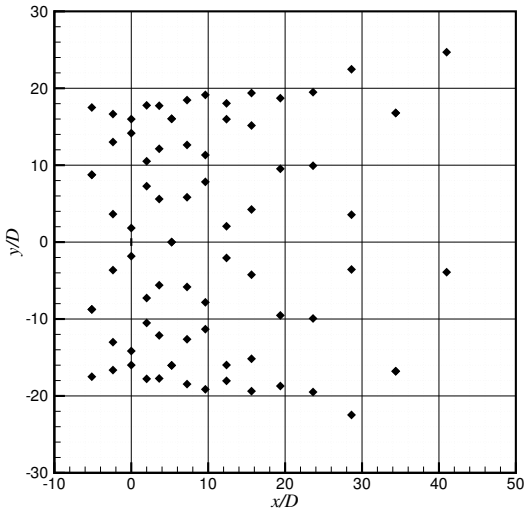


(a) Observer positions projected onto the $x$-$y$ plane.

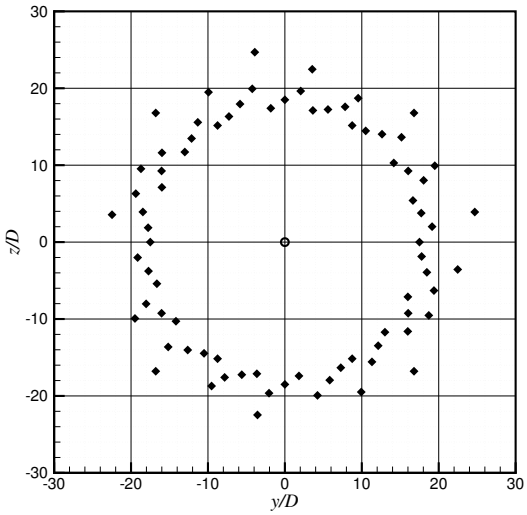


(b) Observer positions projected onto the $y$-$z$ plane.

**Figure 6. Observer positions of the mid-field array.**

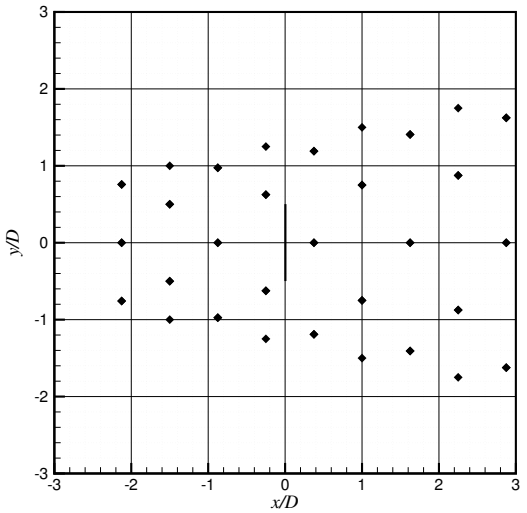


(a) Observer positions projected onto the $x$-$y$ plane.

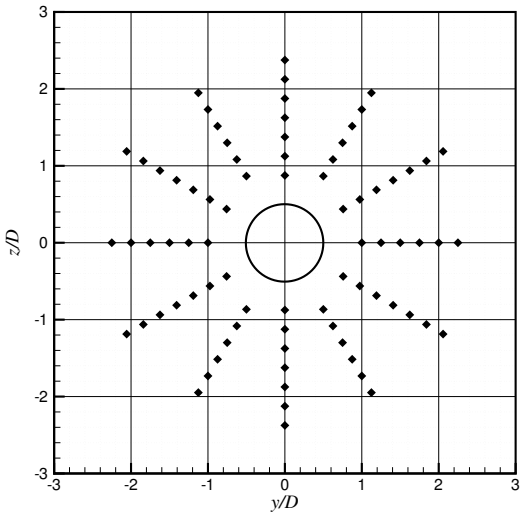


(b) Observer positions projected onto the $y$-$z$ plane.

**Figure 7. Observer positions of the near-field array.**



S. A. E. Miller, Ph.D., s.miller@nasa.gov

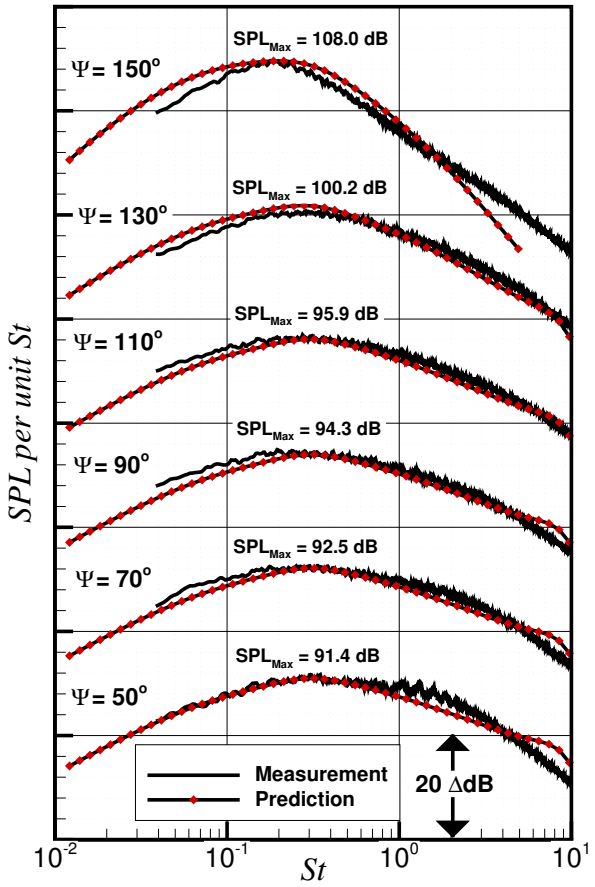


**Figure 8. Far-field SPL per unit $St$ at varying $\Psi$ and $R/D = 100$ from a $M_d = 1.00$, $M_j = 1.00$, and TTR = 1.00 jet.**

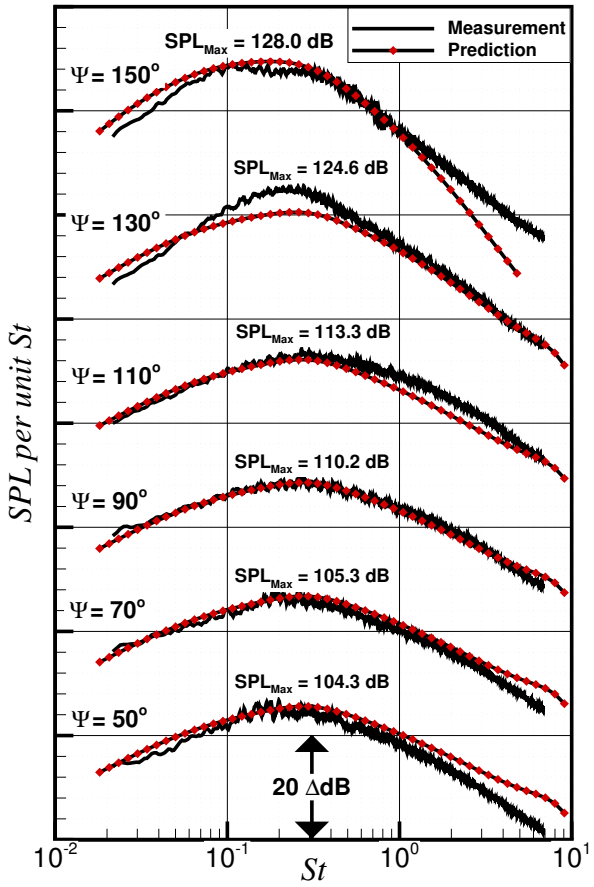


**Figure 9. Far-field SPL per unit $St$ at varying $\Psi$ and $R/D = 100$ from a $M_d = 1.00$, $M_j = 1.00$, and TTR = 3.20 jet.**



S. A. E. Miller, Ph.D., s.miller@nasa.gov

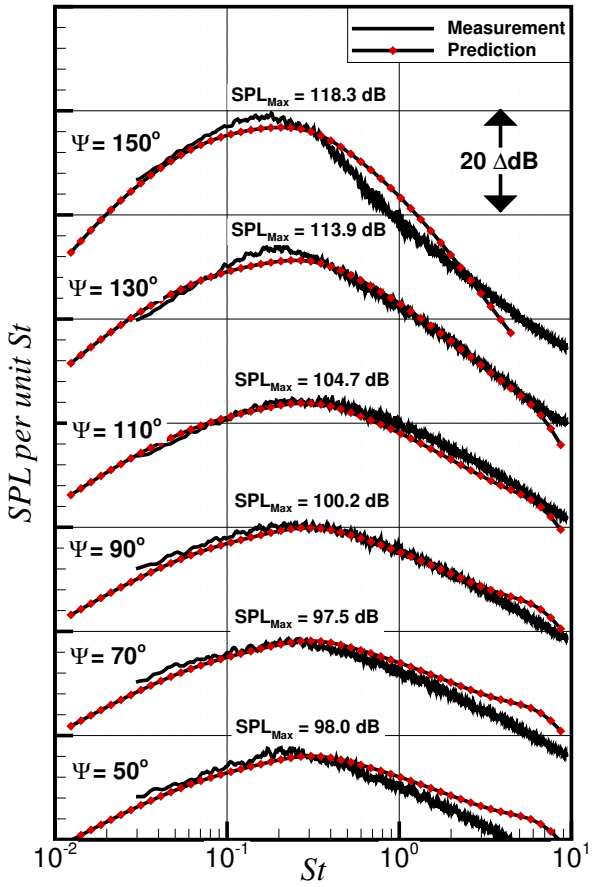


**Figure 10. Far-field SPL per unit $St$ at varying $\Psi$ and $R/D = 100$ from a $M_d = 1.00$, $M_j = 0.70$, and TTR = 3.20 jet.**

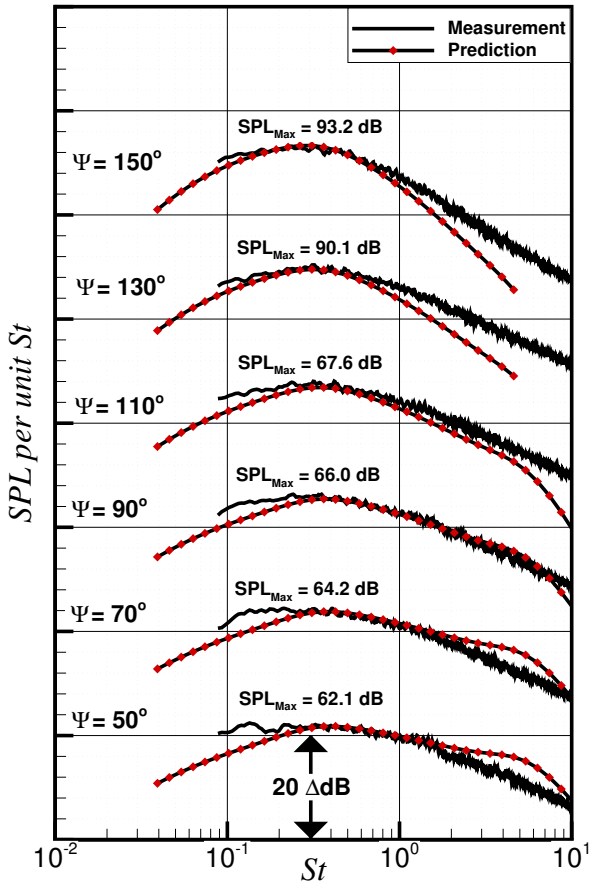


**Figure 11. Far-field SPL per unit $St$ at varying $\Psi$ and $R/D = 100$ from a $M_d = 1.00$, $M_j = 0.40$, and TTR = 1.00 jet.**



S. A. E. Miller, Ph.D., s.miller@nasa.gov

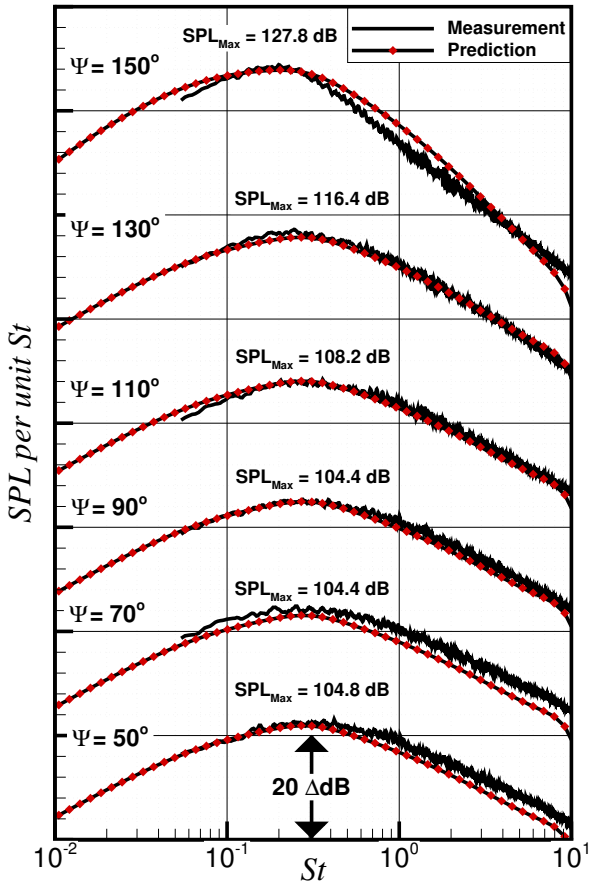


**Figure 12. Far-field SPL per unit $St$ at varying $\Psi$ and $R/D = 100$ from a $M_d = 1.185$, $M_j = 1.185$, and TTR = 1.80 jet.**

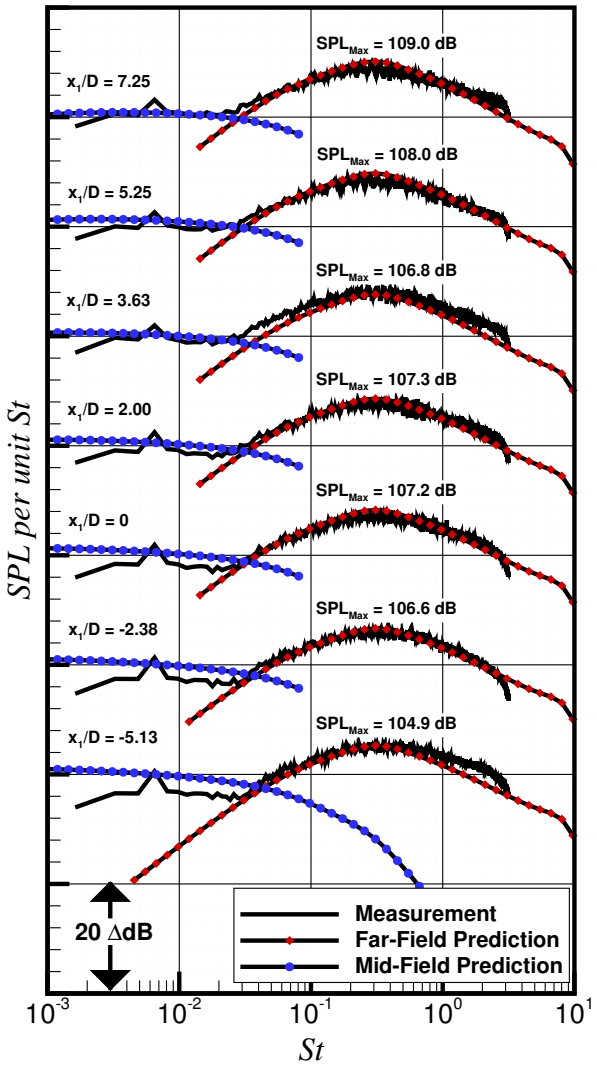


**Figure 13. Mid-field SPL per unit $St$ at varying axial locations from a transonic jet. Observer locations are shown in Table 3 with asterisks for corresponding $x_1/D$.**



S. A. E. Miller, Ph.D., s.miller@nasa.gov

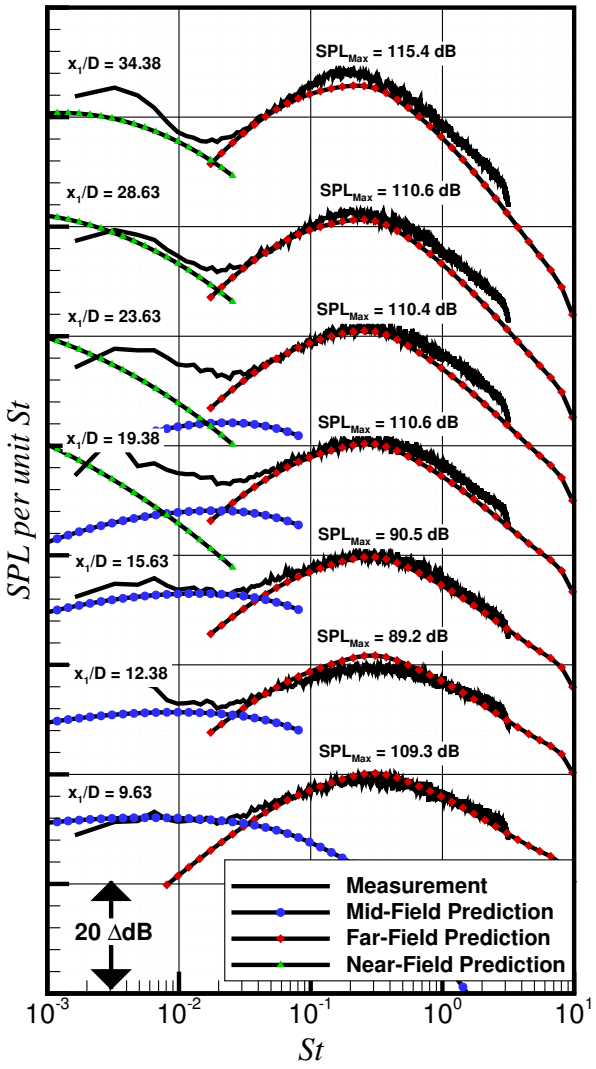


Figure 14. Mid-field SPL per unit $St$ at varying axial locations from a transonic jet. Observer locations are shown in Table 3 with asterisks for corresponding $x_1/D$.

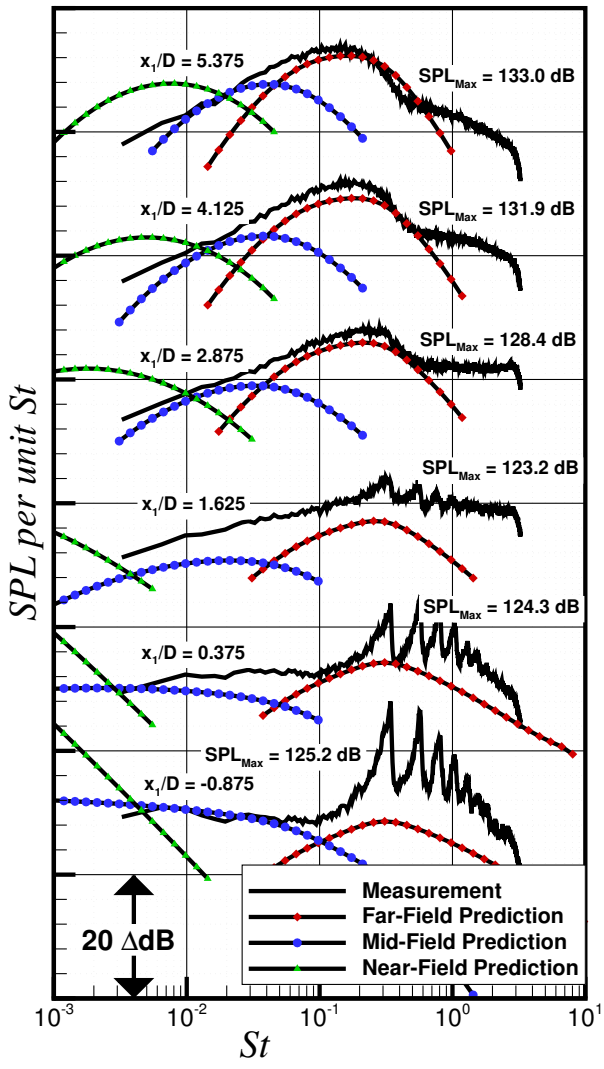


Figure 15. Near-field SPL per unit $St$ at varying axial locations from a transonic jet. Observer locations are shown in Table 4 with asterisks for corresponding $x_1/D$.



S. A. E. Miller, Ph.D., s.miller@nasa.gov

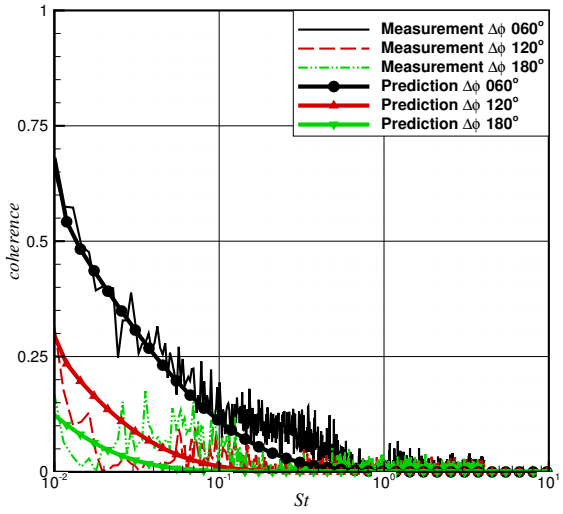


(a) Reference mid-field observer 13 at $x/D = 0$, $y/D = 14.16$, and $z/D = 10.29$.

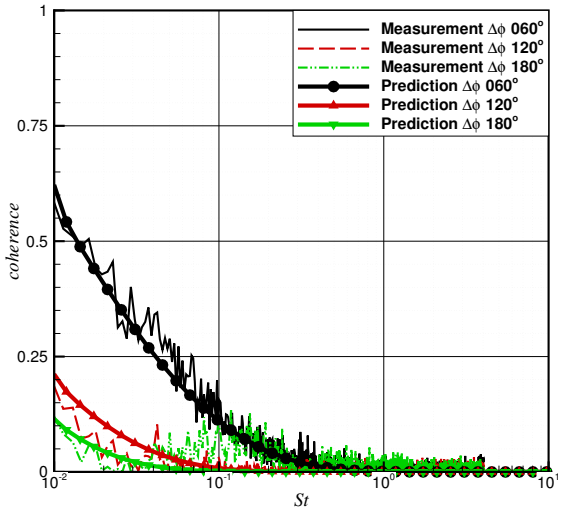


(b) Reference mid-field observer 31 at $x/D = 5.25$, $y/D = 16.03$, and $z/D = 9.25$.

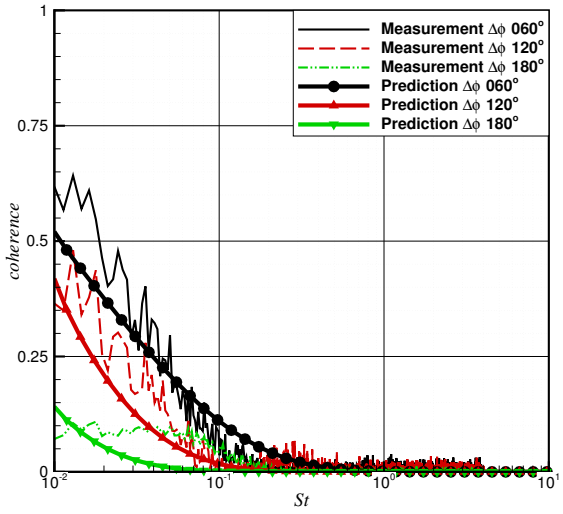


(c) Reference mid-field observer 55 at $x/D = 15.63$, $y/D = 15.16$, and $z/D = 13.63$.

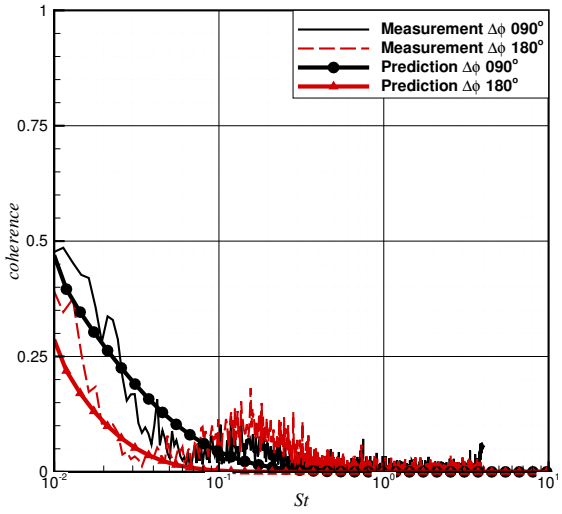


(d) Reference mid-field observer 69 at $x/D = 28.63$, $y/D = 3.56$, and $z/D = 22.47$.

**Figure 16. Mid-field azimuthally varying coherence per unit $St$ referenced to various observer locations from a transonic jet (case SMC0001). Reference Table 3 for observer positions.**



S. A. E. Miller, Ph.D., s.miller@nasa.gov

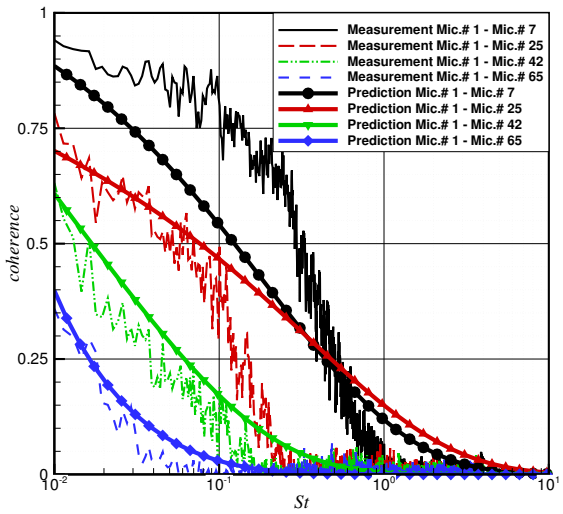


(a) Reference mid-field observer 1 at $x/D$ = -5.13, $y/D$ = 17.50, and $z/D$ = 0.

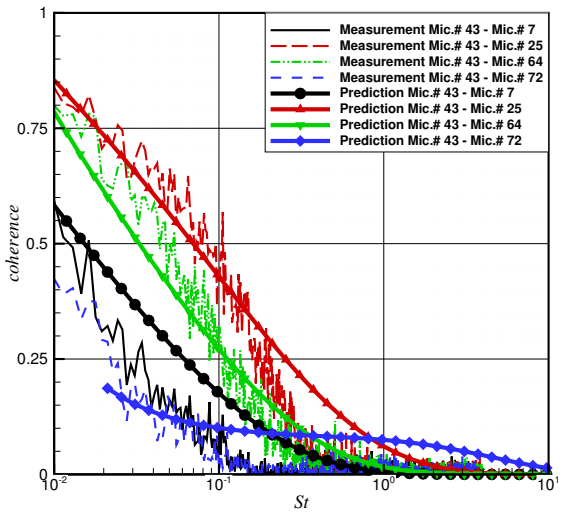


(b) Reference mid-field observer 43 at $x/D$ = 9.63, $y/D$ = 19.14, and $z/D$ = 2.01.

**Figure 17. Mid-field axially varying coherence per unit $St$ referenced to various observer locations from a transonic jet (case SMC0001). Note azimuthal angle also varies. Reference Table 3 for observer positions.**



S. A. E. Miller, Ph.D., s.miller@nasa.gov

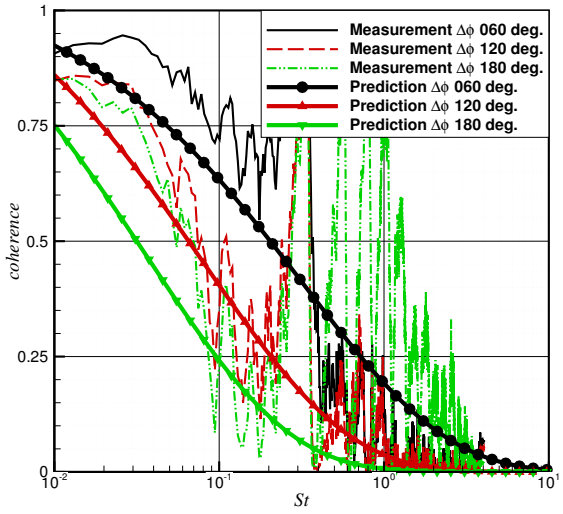


(a) Reference near-field observer 13 at $x/D$ = -0.88, $y/D$ = 0.97, and $z/D$ = 0.56.

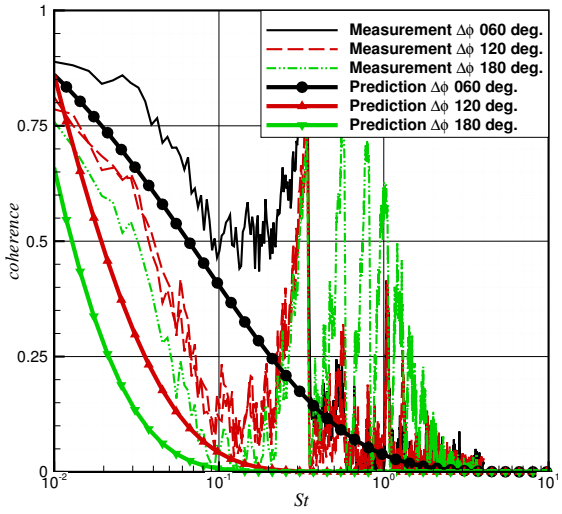


(b) Reference near-field observer 25 at $x/D$ = 0.38, $y/D$ = 1.19, and $z/D$ = 0.69.

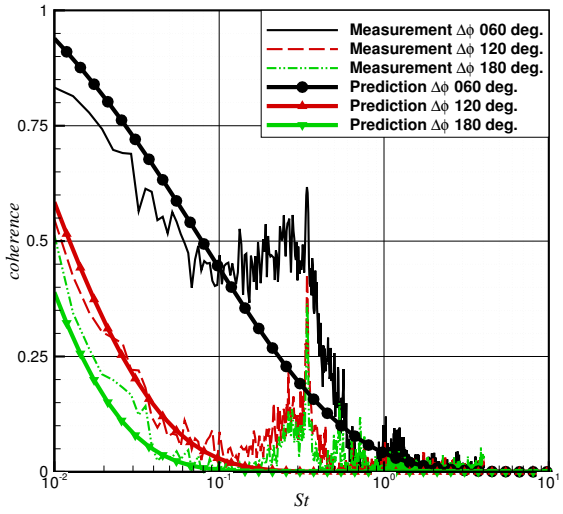


(c) Reference near-field observer 43 at $x/D$ = 2.25, $y/D$ = 1.75, and $z/D$ = 0.

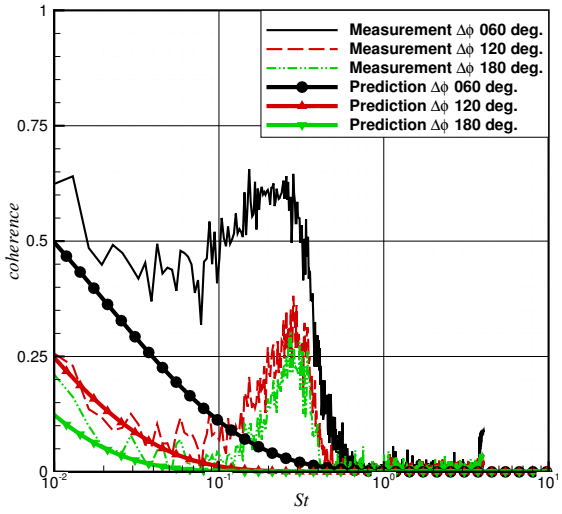


(d) Reference near-field observer 67 at $x/D$ = 4.75, $y/D$ = 2.25, and $z/D$ = 0.

**Figure 18. Near-field azimuthally varying coherence per unit $St$ referenced to various observer locations from a transonic jet (case SMC0001). Reference Table 4 for observer positions.**



S. A. E. Miller, Ph.D., s.miller@nasa.gov

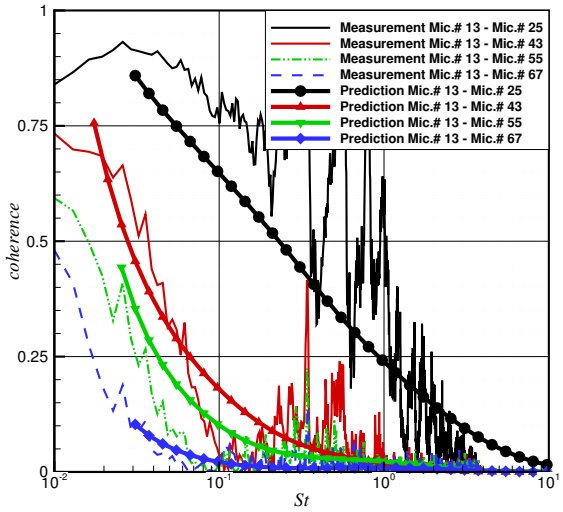


(a) Reference near-field observer 13 at $x/D$ = -0.88, $y/D = 0.97$, and $z/D = 0.56$.

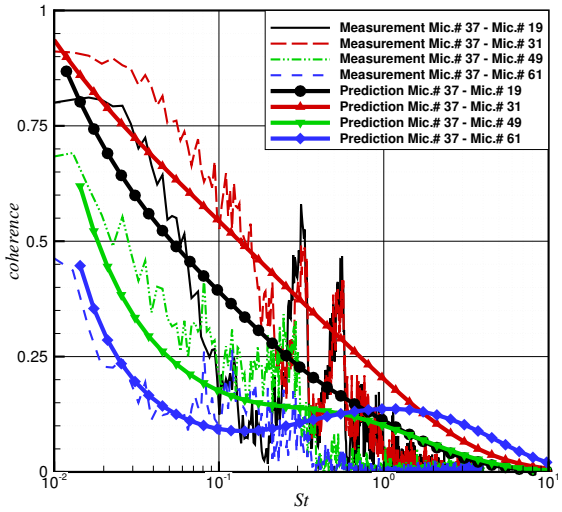


(b) Reference near-field observer 37 at $x/D = 1.63$, $y/D = 1.41$, and $z/D = 0.81$.

**Figure 19. Near-field axially varying coherence per unit $St$ referenced to various observer locations from a transonic jet (case SMC0001). Note azimuthal angle also varies. Reference Table 4 for observer positions.**

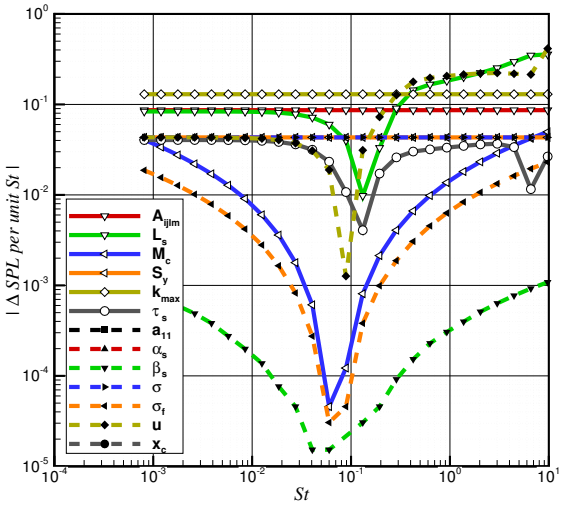


(a) Observer at $x/D = -0.25$, $y/D = 1.25$, and $z/D = 0$.

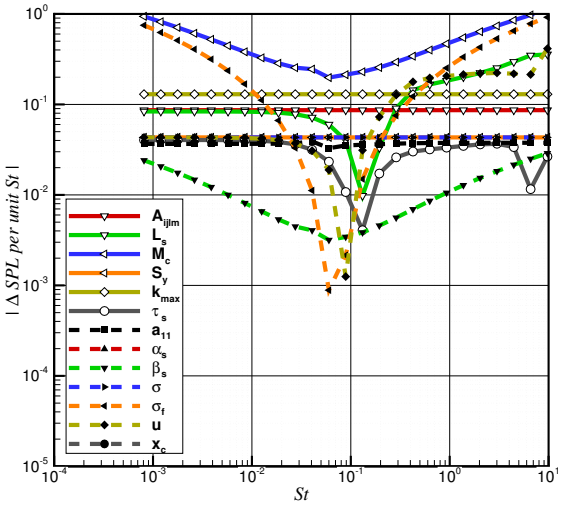


(b) Observer at $x/D = 2.25$, $y/D = 1.75$, and $z/D = 0$.

**Figure 20. Sensitivity of various model parameters as a function of $St$ at two near-field positions.**



S. A. E. Miller, Ph.D., s.miller@nasa.gov

# References


[1]Vaicaitis, R., "Aircraft Cabin Noise Prediction and Optimization," *Final Report - NASA Grant NSG 1450*, 1985.

[2]Thomas, R. H., Burley, C. L., and Olson, E. D., "Hybrid Wing Body Aircraft System Noise Assessment with Propulsion Airframe Aeroacoustic Experiments," *16th AIAA/CEAS Aeroacoustics Conference, Stockholm, Sweden, 7 - 9 June, AIAA Paper 2010-3913*, 2010. doi:10.2514/6.2010-3913.

[3]Czech, M. J., Thomas, R. H., and Elkoby, R., "Propulsion Airframe Aeroacoustic Integration Effects for a Hybrid Wing Body Aircraft Configuration," *16th AIAA/CEAS Aeroacoustics Conference, Stockholm, Sweden, 7 - 9 June, AIAA Paper 2010-3912*, 2010. doi:10.2514/6.2010-3912.

[4]Welge, H. R., Nelson, C., and Bonet, J., "Supersonic Vehicle Systems for the 2020 to 2035 Timeframe," *28th AIAA Applied Aerodynamics Conference, Chicago, Illinois, June 28 - July 1, AIAA Paper 2010-4930*, 2010. doi:10.2514/6.2010-4930.

[5]Welge, H. R., Bonet, J., Magee, T., Chen, D., Hollowell, S., Kutzmann, A., Mortlock, A., Stengle, J., Nelson, C., Adamson, E., Baughcum, S., Britt, R. T., Miller, G., and Tai, J., "N+2 Supersonic Concept Development and Systems Integration," *NASA/CR 2010-216842*, 2010.

[6]Morgenstern, J. M., Stelmach, M., and Jha, P. D., "Advanced Concept Studies for Supersonic Commercial Transports Entering Service in 2030-35 (N+3)," *28th AIAA Applied Aerodynamics Conference, Chicago, Illinois, June 28 - July 1, AIAA Paper 2010-5144*, 2010. doi:10.2514/6.2010-5114.

[7]Seiner, J. M., Manning, J. C., and Ponton, M. K., "Dynamic Pressure Loads Associated with Twin Supersonic Plume Resonance," *AIAA Journal*, Vol. 26, No. 8, 1988, pp. 954–960. doi:10.2514/3.9996.

[8]Miller, S. A. E., Personal communication with U.S. Airforce personnel, 2013.

[9]Haynes, J. and Kenny, R. J., "Modifications to the NASA SP-8072 Distributed Source Method II for Ares I Lift-Off Environment Predictions," *15th AIAA/CEAS Aeroacoustics Conference*, 2009. doi:10.2514/6.2009-3160.

[10]Green, P. D., "Current and Future Problems in Structural Acoustic Fatigue," *AGARD-CP-549: Impact of Acoustic Loads on Aircraft Structures*, May 1994.

[11]Howes, W. L., Callaghan, E. E., Coles, W. D., and Mull, H. R., "Near Noise Field of a Jet-Engine Exhaust," *NACA-TR-1338*, 1976.

[12]Maestrello, L., "Two-Point Correlations of Sound Pressure in the Far Field of a Jet: Experiment," *NASA-TM-X-72835*, 1976.

[13]Juve, D., Sunyach, M., and Comte-Bellot, G., "Filtered Azimuthal Correlations in the Acoustic Far Field of a Subsonic Jet," *AIAA Journal*, Vol. 17, No. 1, 1979, pp. 112–113. doi:10.2514/3.61076.

[14]Kopiev, V. F., Zaitsev, M. Y., Velichko, S. A., Kotova, A. N., and Belyaev, I. V., "Cross-Correlations of Far Field Azimuthal Modes in Subsonic Jet Noise," *14th AIAA/CEAS Aeroacoustics Conference (29th AIAA Aeroacoustics Conference), AIAA Paper 2008-2887*, 2008. doi:10.2514/6.2008-2887.

[15]Ribner, H., "Theory of Two-Point Correlations of Jet Noise," *NASA TN D-8330*, 1976.

[16]Bonnet, C. M. T. and Fisher, M. J., "Correlation Techniques and Modal Decomposition Analysis for the Detection of Azimuthally Coherent Structures in Jet Flow," *Journal of Sound and Vibration*, Vol. 66, No. 4, 1979, pp. 545–555. doi:10.1016/0022-460X(79)90698-9.

[17]Suzuki, T. and Colonius, T., "Identification of Jet Instability Waves and Design of a Microphone Array," *10th AIAA/CEAS Aeroacoustics Conference, AIAA Paper 2008-2960*, 2004. doi:10.2514/6.2004-2960.

[18]Bridges, J. and Brown, C. A., "Validation of the Small Hot Jet Acoustic Rig for Aeroacoustic Research," *11th AIAA/CEAS Aeroacoustics Conference, AIAA Paper 2005-2846*, 2005. doi:10.2514/6.2005-2846.

[19]Lee, S. S. and Bridges, J., "Phased-Array Measurements of Single Flow Hot Jets," *11th AIAA/CEAS Aeroacoustics Conference, AIAA Paper 2005-2842*, 2005. doi:10.2514/6.2005-2842.

[20]Viswanathan, K., "Investigation of Noise Source Mechanisms in Subsonic Jets," *AIAA Journal*, Vol. 46, No. 8, 2008, pp. 2020–2032. doi:10.2514/1.34471.

[21]Billingsley, J. and Kinns, R., "The Acoustic Telescope," *Journal of Sound and Vibration*, Vol. 48, No. 4, 1976, pp. 485–510. doi:10.1016/0022-460X(76)90552-6.

[22]Fisher, M. J., Harper-Bourne, M., and Glegg, S. A. L., "Jet Engine Noise Source Location: The Polar Correlation Technique," *Journal of Sound and Vibration*, Vol. 51, No. 1, 1977, pp. 23–54. doi:10.1016/S0022-460X(77)80111-9.

[23]Doty, M. J. and McLaughlin, D. K., "Space-Time Correlation Measurements of High-Speed Axisymmetric Jets Using Optical Deflectometry," *Experiments in Fluids*, Vol. 38, No. 4, 2005, pp. 415–425. doi:10.1007/s00348-004-0920-1.

[24]Panda, J. and Seasholtz, R. G., "Experimental Investigation of Density Fluctuations in High-Speed Jets and Correlation with Generated Noise," *Journal of Fluid Mechanics*, Vol. 450, 2002, pp. 97–130. doi:10.1017/S002211200100622X.

[25]Panda, J. and Mosher, R., "Microphone Phased Array to Identify Liftoff Noise Sources in Model-Scale Tests," *Journal of Spacecraft and Rockets*, Vol. 50, No. 5, 2013, pp. 1002–1012. doi:10.2514/1.A32433.

[26]Shur, M. L., Spalart, P. R., and Strelets, M. K., "Noise Prediction for Underexpanded Jets in Static and Flight Conditions," *AIAA Journal*, Vol. 49, No. 9, 2011, pp. 2000–2017. doi:10.2514/1.J050776.

[27]Mendez, S., Shoeybi, M., Sharma, A., Ham, F. E., Lele, S. K., and Moin, P., "Large-Eddy Simulations of Perfectly Expanded Supersonic Jets Using an Unstructured Solver," *AIAA Journal*, Vol. 50, No. 5, 2012, pp. 1103–1118. doi:10.2514/1.J051211.

[28]Erwin, J. P., Sinha, N., and Rodebaugh, G. P., "Large Eddy Simulations of Supersonic Impinging Jets," *ASME Turbo Expo 2012: Turbine Technical Conference and Exposition*, Vol. 1, 2012, pp. 449–458. doi:10.1115/GT2012-70140.

[29]Uzun, A. and Hussaini, M. Y., "Simulation of Noise Generation in the Near-Nozzle Region of a Chevron Nozzle Jet," *AIAA Journal*, Vol. 47, No. 8, 2009, pp. 1793–1810. doi:10.2514/1.36659.

[30]Buhler, S., Leonhard, K., and Bogey, C., "Simulation of Subsonic Turbulent Nozzle Jet Flow and Its Near-Field Sound," *AIAA Journal*, 2014. doi:10.2514/1.J052673.

[31]Suzuki, T. and Colonius, T., "Relation Between Instability Waves and Low-Frequency Jet Noise Investigated with Phased-Microphone Arrays," *44th AIAA Aerospace Sciences Meeting and Exhibit, AIAA Paper 2006-622*, 2006. doi:10.2514/6.2006-622.

[32]Suzuki, T., "Noise Sources of Subsonic Round Jets Investigated Using Phased Microphone Arrays," *16th AIAA/CEAS Aeroacoustics Conference, AIAA Paper 2006-3958*, 2010. doi:10.2514/6.2010-3958.

[33]Reba, R., Narayanan, S., Colonius, T., and Suzuki, T., "Modeling Jet Noise from Organized Structures Using Near-Field Hydrodynamic Pressure," *11th AIAA/CLEAS Aeroacoustics Conference, AIAA Paper 2005-3093*, 2005. doi:10.2514/6.2005-3093.

[34]Cavalieri, A., Rodriguez, D., Jordan, P., and Colonius, T., "Wavepackets in the Velocity Field of Turbulent Jets," *18th AIAA/CEAS Aeroacoustics Conference, AIAA Paper 2012-2115*, 2012. doi:10.2514/6.2012-2115.

[35]Lighthill, M. J., "On Sound Generated Aerodynamically. I. General Theory," *Proc. R. Soc. Lond. A.*, Vol. 211, No. 1107, 1952, pp. 564–587. doi:10.1098/rspa.1952.0060.

[36]Lighthill, M. J., "On Sound Generated Aerodynamically. II. Turbulence as a Source of Sound," *Proc. R. Soc. Lond. A.*, Vol. 222, No. 1148, 1954, pp. 1–32. doi:10.1098/rspa.1954.0049.

[37]Richarz, W., "A Theoretical Study of the Coherence of Jet Noise," *6th AIAA Aeroacoustics Conference, AIAA Paper 80-1005*, 1980. doi:10.2514/6.1980-1005.

[38]Harper-Bourne, M., "Jet Near-Field Noise Prediction," *15th Aerodynamic Decelerator Systems Technology Conference*, 1999. doi:10.2514/6.1999-1838.

[39]Lighthill, M. J., "Aerodynamic Noise, or, Turbulence as a Source of Sound," *Fluid Motion Sub-Committee Aeronautical Research Council*, 1950, pp. 1–26.

[40]Ffowcs Williams, J. E., "The Noise from Turbulence Convected at High Speed," *Phil. Trans. R. Soc. Lond. A*, Vol. 255, No. 1063, 1963, pp. 469–503. doi:10.1098/rsta.1963.0010.

[41]Goldstein, M. E., "Aeroacoustics," *NASA SP-346*, 1976.

[42]Tam, C. K. W. and Auriault, L., "Jet Mixing Noise from Fine-Scale Turbulence," *AIAA Journal*, Vol. 37, No. 2, 1999, pp. 145–153.

[43]Morris, P. J. and Farassat, F., "Acoustic Analogy and Alternative Theories for Jet Noise Prediction," *AIAA Journal*, Vol. 40, No. 4, 2002, pp. 671–680.

[44]Miller, S. A. E., "Toward a Comprehensive Model of Jet Noise using an Acoustic Analogy," *AIAA Journal*, 2014. doi:10.2514/1.J052809.

[45]Khavaran, A., "Role of Anisotropy in Turbulent Mixing Noise," *AIAA Journal*, Vol. 37, No. 7, 1999, pp. 832–841.

[46]Lau, J. C., Morris, P. J., and Fisher, M. J., "Measurements in Subsonic and Supersonic Free Jets using a Laser Velocimeter," *Journal of Fluid Mechanics*, Vol. 93, No. 1, 1979, pp. 1–27. doi:10.1017/S0022112079001750.

[47]Lau, J. C., Morris, P. J., and Fisher, M. J., "Effects of Exit Mach Number and Temperature on Mean-Flow and Turbulence Characteristics in Round Jets," *Journal of Fluid Mechanics*, Vol. 105, No. 1, 1981, pp. 193–218. doi:10.1017/S0022112081003170.

[48]Tam, C. K. W., "Broadband Shock-Associated Noise of Moderately Imperfectly Expanded Jets," *Journal of Sound and Vibration*, Vol. 140, No. 1, 1990, pp. 55–71. doi:10.1016/0022-460X(90)90906-G.

[49]Tam, C. K. W., Pastouchenko, N. N., and Schlinker, R. H., "Noise Source Distribution in Supersonic Jets," *Journal of Sound and Vibration*, Vol. 291, No. 1-2, 2006, pp. 192–201. doi:10.1016/j.jsv.2005.06.014.

[50]Schlinker, H. R., "Supersonic Jet Noise Experiments," *PhD Thesis, Department of Aerospace Engineering, University of Southern California*, 1975.

[51]Laufer, S., Schlinker, R., and Kaplan, R. E., "Experiments on Supersonic Jet Noise," *AIAA Journal*, Vol. 14, No. 4, 1976, pp. 489–497. doi:10.2514/3.61388.

[52]Ferguson, W. E., "A Simple Derivation of Glassman's General N Fast Fourier Transform," *Computers and Mathematics with Applications*, Vol. 8, No. 6, 1982, pp. 401–411. doi:10.1016/0898-1221(82)90016-5.

[53]Bass, H. E., Sutherland, L. C., Zuckerwar, A. J., Blackstock, D. T., and Hester, D. M., "Atmospheric Absorption of Sound: Further Developments," *Journal of the Acoustical Society of America*, Vol. 97, No. 1, 1995, pp. 680–683. doi:10.1121/1.412989.

[54]Bass, H. E., Sutherland, L. C., Zuckerwar, A. J., Blackstock, D. T., and Hester, D. M., "Erratum: Atmospheric absorption of sound: Further developments," *Journal of the Acoustical Society of America*, Vol. 99, No. 2, 1996, pp. 1259–1259. doi:10.1121/1.415223.



S. A. E. Miller, Ph.D., s.miller@nasa.gov